Dynamic model of open shell structures buried in poroelastic soils*

J.D.R. Bordón, J.J. Aznárez, O. Maeso
Instituto Universitario de Sistemas Inteligentes y Aplicaciones Numéricas en Ingeniería,
Universidad de Las Palmas de Gran Canaria, Edificio Central del Parque Científico y Tecnológico del
Campus Universitario de Tafira, 35017 Las Palmas de Gran Canaria, Spain
{jdrodriguez,jaznarez,omaeso}@iusiani.ulpgc.es

May 20, 2017

Abstract

This paper is concerned with a three-dimensional time harmonic model of open shell structures buried in poroelastic soils. It combines the Dual Boundary Element Method (DBEM) for treating the soil and shell finite elements for modelling the structure, leading to a simple and efficient representation of buried open shell structures. A new fully regularised Hypersingular Boundary Integral Equation (HBIE) has been developed to this aim, which is then used to build the pair of Dual BIEs necessary to formulate the DBEM for Biot poroelasticity. The new regularised HBIE is validated against a problem with analytical solution. The model is used in a wave diffraction problem in order to show its effectiveness. It offers excellent agreement for length to thickness ratios greater than 10, and relatively coarse meshes. The model is also applied to the calculation of impedances of bucket foundations. It is found that all impedances except the torsional one depend considerably on hydraulic conductivity within the typical frequency range of interest of offshore wind turbines. *Keywords*: dual boundary element method poroelastodynamics shells soil-structure interaction

1 Introduction

The Finite Element Method (FEM) and the Boundary Element Method (BEM) are well known numerical methods that can handle a wide variety of problems [43, 45]. Nevertheless, there are problems where neither the FEM nor the BEM is capable of solving these in an efficient manner. The main advantage of the FEM is its versatility in handling a huge collection of problems that may include structural members (beams, arches, plates, shells), nonlinearities, anisotropy and many other aspects. However, when unbounded domains are present in a wave propagation problem, it requires the truncation of the volume mesh and the presence of some absorbing boundary that help to impose the Sommerfeld radiation condition. Although this has been acceptably solved by Perfectly Matched Layers [4], the BEM is more appealing as it intrinsically satisfies the radiation condition. In this paper, both numerical methods are combined in order to efficiently solve three-dimensional Soil-Structure Interaction problems where the soil is a Biot poroelastic medium and the structure is any open shell structure buried in it.

A buried open shell structure is characterised by being in contact with the same surrounding region on both faces of the shell. On the other hand, a buried closed shell structure, such as a tunnel or a box-like structure, is in contact with different regions on each side of the shell. In both cases, a conventional multi-region BEM approach can be used to deal with the soil and the structure, e.g. [27, 28], but undoubtedly the structure would be more easily handled if treated by the FEM. In the case of closed shell structures, conventional multi-region BEM coupled with shell finite elements can be used [42]. In the case of open shell structures, it can still be used by artificially transforming them into closed ones. However, fictitious (nonphysical) interfaces must be created, e.g. [25], unnecessarily increasing the number of degrees of freedom. In order to obtain an efficient model, we propose a BEM–FEM model where the key idea is using the Dual BEM (DBEM) [21, 35, 39], which is commonly used for crack analysis, to treat the soil–shell interface. This methodology has recently been applied by the authors to two-dimensional Fluid-Structure Interaction [8] and Soil-Structure Interaction [9] problems. Therefore, the aims of this paper are:

- Present a new analytically regularised Hypersingular Boundary Integral Equation (HBIE) for three-dimensional Biot poroelasticity valid for curved elements. The HBIE is then used in combination with the conventional Singular BIE (SBIE) to form the Dual BIE (DBIE) that is used by the DBEM.

- Present the three-dimensional DBEM–FEM (soil-shell) dynamic model for any open shell structure surrounded by a poroelastic medium. The cases of an elastic solid or an inviscid fluid as a surrounding medium can be considered as particular cases of this model.

The rest of the paper is organised as follows. In Section 2, the main aspects of the proposed DBEM–FEM model are described. In particular, the treatment of the poroelastic soil by using the Conventional and the Dual Boundary Element Method is described through Sections 2.1, 2.2 and 2.3. Shell modelling is described in Section 2.4, and BE–FE coupling is described in Section 2.5. Several results are

*The final publication is available at Springer via http://dx.doi.org/10.1007/s00466-017-1406-3

presented in Section 3. The developed regularised HBIE is validated in Section 3.1. In Section 3.2, a wave diffraction problem based on a vibration isolation wall is studied, and the effectiveness of the DBEM–FEM model is analysed. Impedances of bucket foundations installed in sandy soils are obtained and analysed in Section 3.3. Finally, conclusions are given in Section 4

2 Methodology

2.1 Biot poroelasticity

The theory of poroelasticity presented by Biot [6] is able to model the propagation of waves in a two-phase medium consisting of an isotropic elastic solid frame saturated by a compressible viscous fluid. The governing equations in the time domain can be written as:

$$\mu\nabla^2\mathbf{u}+\nabla\left[N\left(\nabla\cdot\mathbf{u}\right)+Q\left(\nabla\cdot\mathbf{U}\right)\right]+\mathbf{X}= \rho_{11}\ddot{\mathbf{u}}+\rho_{12}\ddot{\mathbf{U}}+b\left(\dot{\mathbf{u}}-\dot{\mathbf{U}}\right) \quad (1)$$

$$\nabla\left[Q\left(\nabla\cdot\mathbf{u}\right)+R\left(\nabla\cdot\mathbf{U}\right)\right]+\mathbf{X}'= \rho_{12}\ddot{\mathbf{u}}+\rho_{22}\ddot{\mathbf{U}}-b\left(\dot{\mathbf{u}}-\dot{\mathbf{U}}\right) \quad (2)$$

and the stress-strain relationships as:

$$\tau_{ij}=\delta_{ij}\left[\left(N-\mu\right)\left(\nabla\cdot\mathbf{u}\right)+Q\left(\nabla\cdot\mathbf{U}\right)\right]+\mu\left(u_{i,j}+u_{j,i}\right) \quad (3)$$

$$\tau=Q\left(\nabla\cdot\mathbf{u}\right)+R\left(\nabla\cdot\mathbf{U}\right) \quad (4)$$

where $N=\lambda+\mu+Q^2/R$, $i,j=1,2,3$, u_i and τ_{ij} are respectively the displacements and stresses of the solid phase, U_i and τ the displacements and equivalent stress of the fluid phase, and $\mathbf{X}$ and $\mathbf{X}'$ the body forces of solid and fluid phases. The material properties λ and μ are the Lamé's parameters of the solid phase, Q and R are the Biot's coupling parameters, b is the dissipation constant, and $\rho_{11}=(1-\phi)\rho_\mathrm{s}+\rho_\mathrm{a}$, $\rho_{12}=-\rho_\mathrm{a}$, $\rho_{22}=\phi\rho_\mathrm{f}+\rho_\mathrm{a}$, being ϕ the porosity, ρ_s the solid phase density, ρ_f the fluid phase density, and ρ_a the additional apparent density. The dissipation constant b is related to the hydraulic conductivity k by the relationship $b=\rho_\mathrm{f} g\phi^2/k$, where g is the gravitational acceleration [10]. Assuming a time variation $\exp(i\omega t)$, where ω is the circular frequency, Equations (1-2) become:

$$\mu\nabla^2\mathbf{u}+\nabla\left[N\left(\nabla\cdot\mathbf{u}\right)+Q\left(\nabla\cdot\mathbf{U}\right)\right]+\mathbf{X}= -\omega^2\left(\hat{\rho}_{11}\mathbf{u}+\hat{\rho}_{12}\mathbf{U}\right) \quad (5)$$

$$\nabla\left[Q\left(\nabla\cdot\mathbf{u}\right)+R\left(\nabla\cdot\mathbf{U}\right)\right]+\mathbf{X}'=-\omega^2\left(\hat{\rho}_{12}\mathbf{u}+\hat{\rho}_{22}\mathbf{U}\right) \quad (6)$$

where $\hat{\rho}_{11}=\rho_{11}-ib/\omega$, $\hat{\rho}_{22}=\rho_{22}-ib/\omega$ and $\hat{\rho}_{12}=\rho_{12}+ib/\omega$. From Equations (5-6), it can be obtained that three modes of propagation exists: longitudinal modes P1 and P2, and transverse mode S. The wavenumbers k_P associated with longitudinal modes and the wavenumber k_S associated with the transverse mode are obtained from:

$$k_\mathrm{P}=\pm\sqrt{\frac{a_1\pm\sqrt{a_1^2-4a_0}}{2}},\quad a_0=\omega^4\frac{\hat{\rho}_{11}\hat{\rho}_{22}-\hat{\rho}_{12}^2}{R\left(\lambda+2\mu\right)} \quad (7)$$
$$a_1=\omega^2\left(\frac{\hat{\rho}_{22}}{R}+\frac{\hat{\rho}_{11}+\hat{\rho}_{22}Q^2/R^2-\hat{\rho}_{12}2Q/R}{\lambda+2\mu}\right)$$

and

$$k_\mathrm{S}=\pm\omega\sqrt{\frac{\hat{\rho}_{11}-\hat{\rho}_{12}^2/\hat{\rho}_{22}}{\mu}} \quad (8)$$

where only those with positive real part are considered. The P wavenumber associated with the fastest wave speed is $k_{\mathrm{P}1}$ (solid and fluid dilatation are in phase), while the P wavenumber associated with the slowest wave speed is $k_{\mathrm{P}2}$ (solid and fluid dilatation are out of phase).

2.2 Boundary Integral Equations

The main ingredients of the BEM are the Boundary Integral Equations (BIE), which, after a proper discretisation, are used to build a solvable linear system of equations. In the context of Biot poroelasticity, several BIEs have been proposed [7, 14, 15, 29, 33, 34], which, among other aspects, differ from each other in the selection of the variables. The pore pressure p is often used instead of the fluid equivalent stress (or fluid partial stress) τ, being both related by $\tau=-\phi p$. Likewise, the specific fluid flux $q_i=-\phi(\dot{u}_i-\dot{U}_i)$ or the specific normal fluid flux $q_n=q_j n_j$ is often used instead of the fluid displacements U_i or the normal displacement $U_n=U_j n_j$. The choice is a matter of preference or convenience. The Singular BIE (SBIE) proposed by Domínguez [15] is especially advantageous here as it uses a reduced set of four variables (fluid normal displacement U_n, fluid equivalent stress τ, solid displacements u_k and solid tractions t_k) that leads to simple coupling equations, see Equations (45-46). Domínguez [16] presented the corresponding BEM for two-dimensional problems, while Maeso et al. [27, 28] extended it for three-dimensional problems. Another advantage is that, as done in [28], the fundamental solution can be written in a way that resembles the fundamental solutions of acoustics and elastodynamics, which eases later developments by identifying similar terms. In fact, this strategy is particularly useful in this work for presenting a fully regularised three-dimensional Hypersingular BIE (HBIE) and Dual BIE (DBIE) for Biot poroelasticity valid for curved elements. The regularisation process of these is based on [17], which deals with the elastodynamic problem. The procedure explicitly reduce all strongly singular and hypersingular surface integrals to weakly singular surface integrals and line integrals by making use of the Stokes' theorem. In this sense, we must mention the work of Messner and Schanz, who had already presented a regularised HBIE for collocation BEM [33] and Galerkin BEM [34] for Biot poroelasticity following a similar philosophy.

Let Ω be a poroelastic region, and $\Gamma=\partial\Omega$ its boundary with outward unit normal $\mathbf{n}$. Using the weighted residual formulation proposed by Domínguez [15, 28], the SBIE at

a collocation point $\mathbf{x}^i \notin \Gamma$ can be written as:

$$\delta^i_\Omega \mathbf{I}^i_S \mathbf{u}^i + \int_\Gamma \mathbf{T}^* \mathbf{u}\, d\Gamma = \int_\Gamma \mathbf{U}^* \mathbf{t}\, d\Gamma \tag{9}$$

The vector $\mathbf{u}$ contains all the primary variables: fluid equivalent stress τ and solid displacements u_k; while $\mathbf{t}$ contains all the secondary variables: fluid normal displacement $U_n = U_j n_j$ and solid traction $t_k = \tau_{kj} n_j$. The primary variables at the collocation point are τ^i and u^i_k. The scalar δ^i_Ω takes the value 1 if the collocation point is an interior point ($\mathbf{x}^i \in \Omega$), whereas it is null if the collocation point is an exterior point ($\mathbf{x}^i \notin \Omega \cup \Gamma$). The matrix $\mathbf{I}^i_S$ and the fundamental solution matrices $\mathbf{U}^*$ and $\mathbf{T}^*$ are fully described in Appendix A. All the integrals are regular, although nearly singular due to the presence of terms of order $\mathscr{O}(r^{-p})$ ($r = |\mathbf{x} - \mathbf{x}^i|$, $p \leq 5$). When the collocation point is a boundary point ($\mathbf{x}^i \in \Gamma$), the integrals contain a singularity, and thus the integration domain is taken as the following limit:

$$\Gamma = \lim_{\varepsilon \to 0^+} \left\{ \Gamma^R + \left[\left(\Gamma^S - e^i \right) + \Gamma^i \right] \right\} \tag{10}$$

where Γ^S is a portion of the Γ that contains the singularity, Γ^R is the complementary part of Γ^S, e^i is a circular surface of Γ^S with radius ε centred at the collocation point, and Γ^i is a spherical surface with radius ε centred at the collocation point. The spherical surface can be oriented to the outside (spherical bump) or to the inside (spherical hole) with respect to Ω. In the former, the collocation point is an interior point, while, in the latter, it is an exterior point. After carrying out the integration over the spherical surface, both alternatives lead to the same SBIE:

$$\begin{bmatrix} J c^i_{00} & 0 \\ 0 & c^i_{lk} \end{bmatrix} \mathbf{u}^i + \int_{\Gamma^R} \mathbf{T}^* \mathbf{u}\, d\Gamma + \lim_{\varepsilon \to 0^+} \int_{\Gamma^S - e^i} \mathbf{T}^* \mathbf{u}\, d\Gamma = \int_{\Gamma^R} \mathbf{U}^* \mathbf{t}\, d\Gamma + \lim_{\varepsilon \to 0^+} \int_{\Gamma^S - e^i} \mathbf{U}^* \mathbf{t}\, d\Gamma \tag{11}$$

where $J = 1/(\hat{\rho}_{22}\omega^2)$. For a collocation point located at a general non-smooth boundary point, the free-terms c^i_{00} and c^i_{lk} can be obtained from the closed analytical formulas provided by Mantič [30], being c^i_{00} the potential free-term, and c^i_{lk} the elastostatic free-term with drained properties. The integrals over Γ^R are regular. The integrals over $\Gamma^S - e^i$ are at most weakly singular, except an integral associated with t^*_{lk} that is strongly singular. The fundamental solution t^*_{lk} can be decomposed in such a way that the term that leads to the strongly singular integral is isolated from the rest:

$$t^*_{lk} = t^{*(W)}_{lk} + \frac{\tilde{\mu}}{4\pi} \frac{r_{,l} n_k - r_{,k} n_l}{r^2} = t^{*(W)}_{lk} + t^{*(S)}_{lk} \tag{12}$$

where $\tilde{\mu} = \mu/(\lambda + 2\mu)$. Thus, by using Equation (B.2) and the Stokes' theorem, the strongly singular surface integral is turned into a weakly singular surface integral and a nearly singular line integral over $\Lambda^S = \partial\Gamma^S$:

$$H^{(S)}_l = \frac{\tilde{\mu}}{4\pi} \left[\lim_{\varepsilon \to 0^+} \int_{\Gamma^S - e^i} \frac{r_{,l} n_k - r_{,k} n_l}{r^2} \left(u_k - u^i_k \right) d\Gamma + \left(\varepsilon_{lkj} \int_{\Lambda^S} \frac{\mathbf{e}_j \cdot \mathbf{t}}{r}\, d\Lambda \right) u^i_k \right] \tag{13}$$

where ε_{lkj} is the Levi-Civita symbol, $\mathbf{e}_j$ is the unit vector along x_j axis, and $\mathbf{t}$ is the unit tangent vector at the observation point. Finally, the regularised SBIE for a boundary collocation point can be written as:

$$\mathbf{C}^i \mathbf{u}^i + \int_{\Gamma^R} \mathbf{T}^* \mathbf{u}\, d\Gamma + \lim_{\varepsilon \to 0^+} \int_{\Gamma^S - e^i} \mathbf{T}^{*(W)} \mathbf{u}\, d\Gamma + \begin{Bmatrix} 0 \\ H^{(S)}_l \end{Bmatrix} = \int_{\Gamma^R} \mathbf{U}^* \mathbf{t}\, d\Gamma + \lim_{\varepsilon \to 0^+} \int_{\Gamma^S - e^i} \mathbf{U}^* \mathbf{t}\, d\Gamma \tag{14}$$

The HBIE is built by establishing the secondary variables at the collocation point:

$$U^i_n = U^i_j n^i_j = -J \tau^i_{,j} n^i_j - Z u^i_j n^i_j \tag{15}$$

$$t^i_l = \tau^i_{lj} n^i_j = \left[\lambda u^i_{m,m} \delta_{lj} + \mu \left(u^i_{l,j} + u^i_{j,l} \right) \right] n^i_j + \frac{Q}{R} \tau^i n^i_l \tag{16}$$

where $Z = \hat{\rho}_{12}/\hat{\rho}_{22}$, $\mathbf{n}^i$ is the unit normal vector at the collocation point, and the comma derivative notation denotes $\partial/\partial x^i_k$. Hence, Equations (15-16) require a combination of the SBIE and its derivatives with respect to the coordinates of the collocation point. This fact imposes that the primary variables at the collocation point must have continuous first derivatives, i.e. $\tau(\mathbf{x}^i), u_k(\mathbf{x}^i) \in \mathscr{C}^1$. After carrying out all the required operations, the HBIE at a collocation point $\mathbf{x}^i \notin \Gamma$ can be written as:

$$\delta^i_\Omega \mathbf{I}^i_H \mathbf{t}^i + \int_\Gamma \mathbf{S}^* \mathbf{u}\, d\Gamma = \int_\Gamma \mathbf{D}^* \mathbf{t}\, d\Gamma \tag{17}$$

where the matrix $\mathbf{I}^i_H$ and the fundamental solution matrices $\mathbf{D}^*$ and $\mathbf{S}^*$ are fully written in Appendix A. As with the SBIE, all the integrals are regular in these cases, although the nearly singular terms have higher degrees of singularity ($p \leq 7$). When the collocation point is a boundary point, it is again necessary to take the integration domain presented in Equation (10). The case of a geometrically smooth boundary point is considered here, i.e. e^i is a circle and Γ^i a hemisphere, although non-smooth points could be considered at a considerably greater analytical cost [31]. Given that $\tau(\mathbf{x}^i), u_k(\mathbf{x}^i) \in \mathscr{C}^1$, the primary variables admit the expansion:

$$\tau = \tau^i + \tau^i_{,j} r_j + \mathscr{O}\left(r^2\right) \tag{18}$$

$$u_k = u^i_k + u^i_{k,j} r_j + \mathscr{O}\left(r^2\right) \tag{19}$$

where $\tau^i_{,j}$ and $u^i_{k,j}$ are derivatives of their superficial distribution over Γ. Once the integrals over Γ^i are solved using this expansion and substituted back into Equation (17), the HBIE apparently turns to be unbounded:

$$\frac{1}{2} \mathbf{I}^i_H \mathbf{t}^i + \int_{\Gamma^R} \mathbf{S}^* \mathbf{u}\, d\Gamma + \lim_{\varepsilon \to 0^+} \int_{\Gamma^S - e^i} \mathbf{S}^* \mathbf{u}\, d\Gamma + \mathbf{M}^{\Gamma^i} \mathbf{u} \left(\lim_{\varepsilon \to 0^+} \frac{1}{\varepsilon} \right) = \int_{\Gamma^R} \mathbf{D}^* \mathbf{t}\, d\Gamma + \lim_{\varepsilon \to 0^+} \int_{\Gamma^S - e^i} \mathbf{D}^* \mathbf{t}\, d\Gamma \tag{20}$$

where:

$$\mathbf{M}^{\Gamma^i} = \begin{bmatrix} \frac{J}{2} & 0 \\ 0 & -\frac{\tilde{\mu}}{4} \left[(3\lambda + 4\mu) \delta_{lk} + \lambda n^i_l n^i_k \right] \end{bmatrix} \tag{21}$$

The integral over $\Gamma^{\mathrm{S}} - e^{\mathrm{i}}$ in the right hand side of Equation (20) is essentially similar to that of the left hand side of Equation (11). The term of d^*_{lk} leading to the strongly singular integral can be treated in a similar way:

$$d^*_{lk} = d^{*(\mathrm{W})}_{lk} + \frac{\tilde{\mu}}{4\pi}\frac{\mu}{\lambda+2\mu}\frac{r_{,l}n^{\mathrm{i}}_k - r_{,k}n^{\mathrm{i}}_l}{r^2} = d^{*(\mathrm{W})}_{lk} + d^{*(\mathrm{S})}_{lk} \quad (22)$$

where the regularised integral associated with $d^{*(\mathrm{S})}_{lk}$ is:

$$L^{(\mathrm{S})}_l = \frac{\tilde{\mu}}{4\pi}\left[\lim_{\varepsilon\to 0^+}\int_{\Gamma^{\mathrm{S}}-e^{\mathrm{i}}}\frac{r_{,l}(n^{\mathrm{i}}_k - n_k) - r_{,k}(n^{\mathrm{i}}_l - n_l)}{r^2}t_k\,\mathrm{d}\Gamma + \lim_{\varepsilon\to 0^+}\int_{\Gamma^{\mathrm{S}}-e^{\mathrm{i}}}\frac{r_{,l}n_k - r_{,k}n_l}{r^2}\left(t_k - t^{\mathrm{i}}_k\right)\mathrm{d}\Gamma + \left(\varepsilon_{lkj}\int_{\Lambda^{\mathrm{S}}}\frac{\mathbf{e}_j\cdot\mathbf{t}}{r}\,\mathrm{d}\Lambda\right)t^{\mathrm{i}}_k\right] \quad (23)$$

The integral over $\Gamma^{\mathrm{S}} - e^{\mathrm{i}}$ associated with $\mathbf{S}^*$ in Equation (20) is much more complicated. The integrals associated with s^*_{00} and s^*_{lk} are hypersingular, while the integrals associated with s^*_{0k} and s^*_{l0} are strongly singular. For the latter integrals, s^*_{0k} and s^*_{l0} can be split up into a term leading to weakly singular integrals at most, and a term leading to strongly singular integrals:

$$s^*_{0k} = s^{*(\mathrm{W})}_{0k} + \frac{\tilde{\mu}}{4\pi}\frac{Q}{R}\frac{r_{,k}\left(\mathbf{n}\cdot\mathbf{n}^{\mathrm{i}}\right)}{r^2} = s^{*(\mathrm{W})}_{0k} + s^{*(\mathrm{S})}_{0k} \quad (24)$$

$$s^*_{l0} = s^{*(\mathrm{W})}_{l0} - \frac{\tilde{\mu}}{4\pi}\frac{Q}{R}\frac{r_{,l}\left(\mathbf{n}\cdot\mathbf{n}^{\mathrm{i}}\right)}{r^2} = s^{*(\mathrm{W})}_{l0} + s^{*(\mathrm{S})}_{l0} \quad (25)$$

The integrals associated with $s^{*(\mathrm{S})}_{0k}$ and $s^{*(\mathrm{S})}_{l0}$ are both similar in nature, and can be regularised by using Equation (B.3) and the Stokes' theorem:

$$M^{(\mathrm{S})}_0 = \frac{\tilde{\mu}}{4\pi}\frac{Q}{R}\left[\lim_{\varepsilon\to 0^+}\int_{\Gamma^{\mathrm{S}}-e^{\mathrm{i}}}\frac{r_{,k}\left(\mathbf{n}\cdot\mathbf{n}^{\mathrm{i}}\right)}{r^2}\left(u_k - u^{\mathrm{i}}_k\right)\mathrm{d}\Gamma + \left(-\lim_{\varepsilon\to 0^+}\int_{\Gamma^{\mathrm{S}}-e^{\mathrm{i}}}\frac{n_k}{r^2}\frac{\partial r}{\partial n^{\mathrm{i}}}\,\mathrm{d}\Gamma + \int_{\Lambda^{\mathrm{S}}}\frac{\left(\mathbf{e}_k\times\mathbf{n}^{\mathrm{i}}\right)\cdot\mathbf{t}}{r}\,\mathrm{d}\Lambda\right)u^{\mathrm{i}}_k\right] \quad (26)$$

$$M^{(\mathrm{S})}_l = -\frac{\tilde{\mu}}{4\pi}\frac{Q}{R}\left[\lim_{\varepsilon\to 0^+}\int_{\Gamma^{\mathrm{S}}-e^{\mathrm{i}}}\frac{r_{,l}\left(\mathbf{n}\cdot\mathbf{n}^{\mathrm{i}}\right)}{r^2}\left(\tau - \tau^{\mathrm{i}}\right)\mathrm{d}\Gamma + \left(-\lim_{\varepsilon\to 0^+}\int_{\Gamma^{\mathrm{S}}-e^{\mathrm{i}}}\frac{n_l}{r^2}\frac{\partial r}{\partial n^{\mathrm{i}}}\,\mathrm{d}\Gamma + \int_{\Lambda^{\mathrm{S}}}\frac{\left(\mathbf{e}_l\times\mathbf{n}^{\mathrm{i}}\right)\cdot\mathbf{t}}{r}\,\mathrm{d}\Lambda\right)\tau^{\mathrm{i}}\right] \quad (27)$$

The hypersingular integrals associated with s^*_{00} and s^*_{lk} can be treated in a similar way. The fundamental solution s^*_{00} can be split up in order to isolate the term leading to the hypersingular integral:

$$s^*_{00} = s^{*(\mathrm{W})}_{00} + \frac{J}{4\pi}\frac{\mathbf{n}\cdot\mathbf{n}^{\mathrm{i}}}{r^3} = s^{*(\mathrm{W})}_{00} + s^{*(\mathrm{H})}_{00} \quad (28)$$

The hypersingular integral associated with $s^{*(\mathrm{H})}_{00}$ can be regularised by using Equations (18), (B.1) and (B.3), and the Stokes' theorem:

$$M^{(\mathrm{H})}_0 = \frac{J}{4\pi}\left[\lim_{\varepsilon\to 0^+}\int_{\Gamma^{\mathrm{S}}-e^{\mathrm{i}}}\frac{\mathbf{n}\cdot\mathbf{n}^{\mathrm{i}}}{r^3}\left(\tau - \tau^{\mathrm{i}} - \tau^{\mathrm{i}}_{,j}r_j\right)\mathrm{d}\Gamma + \left(-\lim_{\varepsilon\to 0^+}\int_{\Gamma^{\mathrm{S}}-e^{\mathrm{i}}}\frac{3}{r^3}\frac{\partial r}{\partial n}\frac{\partial r}{\partial n^{\mathrm{i}}}\,\mathrm{d}\Gamma + \int_{\Lambda^{\mathrm{S}}}\frac{\left(\mathbf{r}\times\mathbf{n}^{\mathrm{i}}\right)\cdot\mathbf{t}}{r^3}\,\mathrm{d}\Lambda\right)\tau^{\mathrm{i}} + \left(-\lim_{\varepsilon\to 0^+}\int_{\Gamma^{\mathrm{S}}-e^{\mathrm{i}}}\frac{n_j}{r^2}\frac{\partial r}{\partial n^{\mathrm{i}}}\,\mathrm{d}\Gamma + \int_{\Lambda^{\mathrm{S}}}\frac{\left(\mathbf{e}_j\times\mathbf{n}^{\mathrm{i}}\right)\cdot\mathbf{t}}{r}\,\mathrm{d}\Lambda\right)\tau^{\mathrm{i}}_{,j}\right] + \frac{J}{2}\tau^{\mathrm{i}}\left(\lim_{\varepsilon\to 0^+}\frac{1}{\varepsilon}\right) = M^{(\mathrm{Hb})}_0 + \frac{J}{2}\tau^{\mathrm{i}}\left(\lim_{\varepsilon\to 0^+}\frac{1}{\varepsilon}\right) \quad (29)$$

In order to treat the integral associated with s^*_{lk}, it is split up into three parts: a part leading to weakly singular integrals at most, a part leading to a hypersingular integral basically similar to Equation (29), and a part leading to a much more involved hypersingular integral:

$$s^*_{lk} = s^{*(\mathrm{W})}_{lk} + s^{*(\mathrm{H1})}_{lk} + s^{*(\mathrm{H2})}_{lk} = s^{*(\mathrm{W})}_{lk} + \frac{\mu}{4\pi}2\tilde{\mu}\delta_{lk}\frac{\mathbf{n}\cdot\mathbf{n}^{\mathrm{i}}}{r^3} + \frac{\mu}{4\pi}\left[3\tilde{\lambda}\left(\frac{r_{,l}n^{\mathrm{i}}_k}{r^3}\frac{\partial r}{\partial n} - \frac{r_{,k}n_l}{r^3}\frac{\partial r}{\partial n^{\mathrm{i}}} + \frac{r_{,l}r_{,k}\left(\mathbf{n}\cdot\mathbf{n}^{\mathrm{i}}\right)}{r^3}\right) + 6\tilde{\mu}\left(\frac{r_{,k}n^{\mathrm{i}}_l}{r^3}\frac{\partial r}{\partial n} - \frac{r_{,l}n_k}{r^3}\frac{\partial r}{\partial n^{\mathrm{i}}}\right) + 2\tilde{\mu}\frac{n_l n^{\mathrm{i}}_k}{r^3} + 2\left(\tilde{\lambda}-\tilde{\mu}\right)\frac{n_k n^{\mathrm{i}}_l}{r^3}\right] \quad (30)$$

where $\tilde{\lambda} = \lambda/(\lambda+2\mu)$. The regularisation of the hypersingular integral associated with $s^{*(\mathrm{H1})}_{lk}$ gives:

$$M^{(\mathrm{H1})}_l = \frac{\mu}{4\pi}2\tilde{\mu}\delta_{lk}\left[\lim_{\varepsilon\to 0^+}\int_{\Gamma^{\mathrm{S}}-e^{\mathrm{i}}}\frac{\mathbf{n}\cdot\mathbf{n}^{\mathrm{i}}}{r^3}\left(u_k - u^{\mathrm{i}}_k - u^{\mathrm{i}}_{k,j}r_j\right)\mathrm{d}\Gamma + \left(-\lim_{\varepsilon\to 0^+}\int_{\Gamma^{\mathrm{S}}-e^{\mathrm{i}}}\frac{3}{r^3}\frac{\partial r}{\partial n}\frac{\partial r}{\partial n^{\mathrm{i}}}\,\mathrm{d}\Gamma + \int_{\Lambda^{\mathrm{S}}}\frac{\left(\mathbf{r}\times\mathbf{n}^{\mathrm{i}}\right)\cdot\mathbf{t}}{r^3}\,\mathrm{d}\Lambda\right)u^{\mathrm{i}}_k + \left(-\lim_{\varepsilon\to 0^+}\int_{\Gamma^{\mathrm{S}}-e^{\mathrm{i}}}\frac{n_j}{r^2}\frac{\partial r}{\partial n^{\mathrm{i}}}\,\mathrm{d}\Gamma + \int_{\Lambda^{\mathrm{S}}}\frac{\left(\mathbf{e}_j\times\mathbf{n}^{\mathrm{i}}\right)\cdot\mathbf{t}}{r}\,\mathrm{d}\Lambda\right)u^{\mathrm{i}}_{k,j}\right] + \mu\tilde{\mu}\delta_{lk}u^{\mathrm{i}}_k\left(\lim_{\varepsilon\to 0^+}\frac{1}{\varepsilon}\right) = M^{(\mathrm{H1b})}_l + \mu\tilde{\mu}\delta_{lk}u^{\mathrm{i}}_k\left(\lim_{\varepsilon\to 0^+}\frac{1}{\varepsilon}\right) \quad (31)$$

The regularisation process of the hypersingular integral associated with $s^{*(\mathrm{H2})}_{lk}$ starts by using the expansion of u_k given in Equation (19):

$$M^{(\mathrm{H2})}_l = \lim_{\varepsilon\to 0^+}\int_{\Gamma^{\mathrm{S}}-e^{\mathrm{i}}}s^{*(\mathrm{H2})}_{lk}\left(u_k - u^{\mathrm{i}}_k - u^{\mathrm{i}}_{k,j}r_j\right)\mathrm{d}\Gamma + \left(\lim_{\varepsilon\to 0^+}\int_{\Gamma^{\mathrm{S}}-e^{\mathrm{i}}}s^{*(\mathrm{H2})}_{lk}\mathrm{d}\Gamma\right)u^{\mathrm{i}}_k + \left(\lim_{\varepsilon\to 0^+}\int_{\Gamma^{\mathrm{S}}-e^{\mathrm{i}}}r_j s^{*(\mathrm{H2})}_{lk}\mathrm{d}\Gamma\right)u^{\mathrm{i}}_{k,j} = M^{(\mathrm{H21})}_l + M^{(\mathrm{H22})}_l + M^{(\mathrm{H23})}_l \quad (32)$$

where the integral $M^{(\mathrm{H21})}_l$ is weakly singular, $M^{(\mathrm{H22})}_l$ is hypersingular, and $M^{(\mathrm{H23})}_l$ is strongly singular. The hypersingular integral $M^{(\mathrm{H22})}_l$ is regularised by using Equations

(B.4) and (B.5), and the Stokes' theorem, which gives:

$$M_l^{(\mathrm{H22})} = \frac{\mu}{4\pi}\left\{\lim_{\varepsilon\to 0^+}\int_{\Gamma^{\mathrm{S}}-e^{\mathrm{i}}}\left[3\tilde{\lambda}\frac{r_{,k}}{r^3}\left(n_l^{\mathrm{i}}\frac{\partial r}{\partial n}-n_l\frac{\partial r}{\partial n^{\mathrm{i}}}\right)+\right.\right.$$
$$6\tilde{\mu}\frac{r_{,l}}{r^3}\left(n_k^{\mathrm{i}}\frac{\partial r}{\partial n}-n_k\frac{\partial r}{\partial n^{\mathrm{i}}}\right)-15\tilde{\lambda}\frac{r_{,l}r_{,k}}{r^3}\frac{\partial r}{\partial n}\frac{\partial r}{\partial n^{\mathrm{i}}}\Big]\,\mathrm{d}\Gamma+$$
$$3\tilde{\lambda}\int_{\Lambda^{\mathrm{S}}}\frac{r_{,l}r_{,k}\left(\mathbf{r}\times\mathbf{n}^{\mathrm{i}}\right)\cdot\mathbf{t}}{r^3}\,\mathrm{d}\Lambda+2\tilde{\mu}n_k^{\mathrm{i}}\int_{\Lambda^{\mathrm{S}}}\frac{(\mathbf{r}\times\mathbf{e}_l)\cdot\mathbf{t}}{r^3}\,\mathrm{d}\Lambda+$$
$$\left.2\left(\tilde{\lambda}-\tilde{\mu}\right)n_l^{\mathrm{i}}\int_{\Lambda^{\mathrm{S}}}\frac{(\mathbf{r}\times\mathbf{e}_k)\cdot\mathbf{t}}{r^3}\,\mathrm{d}\Lambda\right\}u_k^{\mathrm{i}}+$$
$$\frac{\tilde{\mu}\lambda}{4}\left(3\delta_{lk}+n_l^{\mathrm{i}}n_k^{\mathrm{i}}\right)u_k^{\mathrm{i}}\left(\lim_{\varepsilon\to 0^+}\frac{1}{\varepsilon}\right)=$$
$$M_l^{(\mathrm{H22b})}+\frac{\tilde{\mu}\lambda}{4}\left(3\delta_{lk}+n_l^{\mathrm{i}}n_k^{\mathrm{i}}\right)u_k^{\mathrm{i}}\left(\lim_{\varepsilon\to 0^+}\frac{1}{\varepsilon}\right)\qquad(33)$$

The strongly singular integral $M_l^{(\mathrm{H23})}$ is regularised by using Equation (B.6), then adding and subtracting respectively $n_l^{\mathrm{i}}\left(\mathbf{n}\cdot\mathbf{n}^{\mathrm{i}}\right)$ and $n_k^{\mathrm{i}}\left(\mathbf{n}\cdot\mathbf{n}^{\mathrm{i}}\right)$ from some of the n_l and n_k terms, and eventually using Equation (B.3) and the Stokes' theorem:

$$M_l^{(\mathrm{H23})} = \frac{\mu}{4\pi}\left\{\lim_{\varepsilon\to 0^+}\int_{\Gamma^{\mathrm{S}}-e^{\mathrm{i}}}\left[3\tilde{\lambda}r_{,j}\left(\frac{r_{,l}n_k^{\mathrm{i}}}{r^2}\frac{\partial r}{\partial n}-\frac{r_{,k}n_l}{r^2}\frac{\partial r}{\partial n^{\mathrm{i}}}\right)+\right.\right.$$
$$6\tilde{\mu}r_{,j}\left(\frac{r_{,k}n_l^{\mathrm{i}}}{r^2}\frac{\partial r}{\partial n}-\frac{r_{,l}n_k}{r^2}\frac{\partial r}{\partial n^{\mathrm{i}}}\right)-\tilde{\lambda}\frac{r_{,j}r_{,l}n_k}{r^2}\frac{\partial r}{\partial n^{\mathrm{i}}}+$$
$$\tilde{\lambda}\frac{\left(r_{,j}n_l^{\mathrm{i}}-r_{,l}n_j^{\mathrm{i}}\right)\left(n_k-n_k^{\mathrm{i}}\left(\mathbf{n}\cdot\mathbf{n}^{\mathrm{i}}\right)\right)}{r^2}+2\tilde{\mu}r_{,j}\frac{n_l n_k^{\mathrm{i}}-n_k n_l^{\mathrm{i}}}{r^2}-$$
$$\tilde{\lambda}\left(\left(\delta_{lk}+n_l^{\mathrm{i}}n_k^{\mathrm{i}}\right)n_j+\left(\delta_{jk}-n_j^{\mathrm{i}}n_k^{\mathrm{i}}\right)n_l\right)\frac{1}{r^2}\frac{\partial r}{\partial n^{\mathrm{i}}}\Big]\,\mathrm{d}\Gamma+$$
$$\tilde{\lambda}\left[\left(\delta_{lk}+n_l^{\mathrm{i}}n_k^{\mathrm{i}}\right)\int_{\Lambda^{\mathrm{S}}}\frac{\left(\mathbf{e}_j\times\mathbf{n}^{\mathrm{i}}\right)\cdot\mathbf{t}}{r}\,\mathrm{d}\Lambda+\right.$$
$$\left(\delta_{jk}-n_j^{\mathrm{i}}n_k^{\mathrm{i}}\right)\int_{\Lambda^{\mathrm{S}}}\frac{\left(\mathbf{e}_l\times\mathbf{n}^{\mathrm{i}}\right)\cdot\mathbf{t}}{r}\,\mathrm{d}\Lambda+$$
$$\left.\left.\int_{\Lambda^{\mathrm{S}}}\frac{r_{,l}r_{,j}\left(\mathbf{e}_k\times\mathbf{n}^{\mathrm{i}}\right)\cdot\mathbf{t}}{r}\,\mathrm{d}\Lambda\right]\right\}u_{k,j}^{\mathrm{i}}\qquad(34)$$

After developing the integrals over $\Gamma^{\mathrm{S}}-e^{\mathrm{i}}$ of Equation (20) throughout Equations (22-34), these can be substituted back into Equation (20) to obtain a fully regularised HBIE:

$$\frac{1}{2}\mathbf{I}_{\mathrm{H}}^{\mathrm{i}}\mathbf{t}^{\mathrm{i}}+\int_{\Gamma^{\mathrm{R}}}\mathbf{S}^{o}*\mathbf{u}\,\mathrm{d}\Gamma+\lim_{\varepsilon\to 0^+}\int_{\Gamma^{\mathrm{S}}-e^{\mathrm{i}}}\mathbf{S}^{*(\mathrm{W})}\mathbf{u}\,\mathrm{d}\Gamma+$$
$$\left\{\begin{array}{c}-M_0^{(\mathrm{S})}-M_0^{(\mathrm{Hb})}\\ M_l^{(\mathrm{H1b})}+M_l^{(\mathrm{H22b})}+M_l^{(\mathrm{H23})}\end{array}\right\}=$$
$$\int_{\Gamma^{\mathrm{R}}}\mathbf{D}^{*}\mathbf{t}\,\mathrm{d}\Gamma+\lim_{\varepsilon\to 0^+}\int_{\Gamma^{\mathrm{S}}-e^{\mathrm{i}}}\mathbf{D}^{*(\mathrm{W})}\mathbf{t}\,\mathrm{d}\Gamma+\left\{\begin{array}{c}0\\ L_l^{(\mathrm{S})}\end{array}\right\}\qquad(35)$$

due to the cancellation of all unbounded terms appearing in Equations (29), (31) and (33) with the unbounded term appearing in Equation (20).

The SBIE and HBIE presented respectively in Equations (14) and (35) correspond to collocation points located at ordinary boundaries, with the condition that $\Gamma(\mathbf{x}^{\mathrm{i}})\in\mathscr{C}^1$ and $\mathbf{u}^{\mathrm{i}}\in\mathscr{C}^1$ for the HBIE. When the collocation point is located at a crack-like boundary, both BIEs have to be accordingly modified, but the main issues have already been solved. A crack-like boundary is composed by two ordinary sub-boundaries geometrically coincident but with opposite orientations, denoted as positive $+$ and negative $-$ faces. Taking into account this, the SBIE and HBIE for a given crack-like boundary collocation point $\mathbf{x}^{\mathrm{i}}$ can be written as:

$$\frac{1}{2}\mathbf{I}_{\mathrm{S}}^{\mathrm{i}}\left(\mathbf{u}^{\mathrm{i}+}+\mathbf{u}^{\mathrm{i}-}\right)+\oint_{\Gamma}\mathbf{T}^{*}\mathbf{u}\,\mathrm{d}\Gamma=\int_{\Gamma}\mathbf{U}^{*}\mathbf{t}\,\mathrm{d}\Gamma\qquad(36)$$
$$\frac{1}{2}\mathbf{I}_{\mathrm{H}}^{\mathrm{i}}\left(\mathbf{t}^{\mathrm{i}+}-\mathbf{t}^{\mathrm{i}-}\right)+\oint\!\!\!\!\!\!=_{\Gamma}\mathbf{S}^{*}\mathbf{u}\,\mathrm{d}\Gamma=\oint_{\Gamma}\mathbf{D}^{*}\mathbf{t}\,\mathrm{d}\Gamma\qquad(37)$$

where it has been assumed that $\Gamma(\mathbf{x}^{\mathrm{i}})\in\mathscr{C}^1$, and the Cauchy Principal Value (CPV) ($\int$) and Hadamard Finite Part (HFP) ($\oint\!\!\!\!\!\!=$) notations are used. Although the CPV and HFP concepts are the underlying abstractions behind the regularisation, they have not been used since the presented approach deals explicitly with the singularities and thus directly gives the finite parts. However, these concepts are used in Equations (36) and (37) for the sake of brevity. Both Equations (36) and (37) have to be used simultaneously in order to solve problems with crack-like boundaries. They are best known as Dual BIEs [21], and their application to the BEM is called the Dual BEM [35, 39].

2.3 Boundary Element Method

In this section, the relevant aspects of the implementation of the BEM used in this work are briefly described. The discretisation is performed using classical continuous isoparametric Lagrange elements. Two classes of boundary elements are considered: ordinary (or conventional) and crack-like. In order to build up a solvable linear system of equations, an appropriate collocation of Boundary Integral Equations (14) and/or (35) is done throughout ordinary boundary elements, whereas the collocation of Dual Boundary Integral Equations (36) and (37) is done throughout crack-like boundary elements.

Hypersingular Boundary Integral Equations (35) and (37) impose one important restriction on the choice of elements for the discretisation: the collocation point must be in a point where the primary variables are differentiable, i.e. $\mathbf{u}(\mathbf{x}^{\mathrm{i}})\in\mathscr{C}^1$. A typical solution used in crack analysis is to make use of discontinuous elements [35, 39], where nodes are located inside the elements and hence nodal collocation meets automatically this requirement. However, the usage of continuous boundary elements is more appropriate in this work for two reasons: they can be directly and efficiently coupled to most classical shell finite elements, and the continuity requirement can be avoided by using the Multiple Collocation Approach (MCA) [3, 17, 19].

Consider a node κ shared by N continuous boundary elements. For a given boundary element e, the node κ has the local index k. MCA consists in building a BIE associated with κ by adding several BIEs, one BIE per each element e containing the node with a collocation point $\mathbf{x}^{\mathrm{i}}$ located towards inside the element at a local coordinate $\boldsymbol{\xi}_k^{\mathrm{i}}$. The local coordinate $\boldsymbol{\xi}_k^{\mathrm{i}}$ of the interior collocation point can be controlled by the dimensionless displacement parameter

$\delta \in (0,1)$, which allows calculating $\mathbf{x}^{\mathrm{i}}$ as:

$$\mathbf{x}^{\mathrm{i}} = \mathbf{x}^{\mathrm{i}}(\boldsymbol{\xi}_k^{\mathrm{i}}) \text{ for } \begin{cases} \square \text{ elements: } \boldsymbol{\xi}_k^{\mathrm{i}} = (1-\delta)\,\boldsymbol{\xi}_k \\ \triangle \text{ elements: } \boldsymbol{\xi}_k^{\mathrm{i}} = (1-\delta)\,\boldsymbol{\xi}_k + \dfrac{\delta}{3} \end{cases} \tag{38}$$

where $\boldsymbol{\xi}_k$ is the local coordinate of the node k of the element. Therefore, the BIE for the node κ is obtained from:

$$\mathrm{BIE}_\kappa = \sum_{e=1}^{e=N} \mathrm{BIE}_k^e \left(\mathbf{x}^{\mathrm{i}}(\boldsymbol{\xi}_k^{\mathrm{i}}) \right) \tag{39}$$

For crack-like boundary elements, where MCA is applied on every node, appropriate values of δ are those that produce collocation points located near Gaussian points ($\delta = 0.42$ for linear elements and $\delta = 0.23$ for quadratic elements). This is often used in the literature related to discontinuous and semi-discontinuous elements [32, 43], and also leads to satisfactory results in this case [3].

MCA can also be used to solve the indeterminacy present when using multiple nodes, being only used at those nodes. Appropriate values of δ in this case are not that clear. If δ is relatively big, e.g. $\delta = 0.3$, then the indeterminacy problem is clearly solved, but the continuity of the primary variable across the multiple nodes is compromised. On the other hand, if δ is relatively small, e.g. $\delta = 0.001$, the primary variable is nearly continuous, but the condition number of the resulting linear system of equations could become too big, and also numerical integration issues could appear due to highly quasi-singular integrals. For those reasons, an intermediate value of $\delta = 0.05$ is considered in this work.

2.4 Shell structure

The shell structure is modelled using shell finite elements based on the degenerated solid approach [1]. These classical shell elements are versatile and relatively easy to handle. Their major drawback is the presence of shear and membrane locking, which are due to the inability of the displacement interpolation to represent thin shell (vanishing out-of-plane shear stresses in bending) and curved shell (vanishing in-plane stresses in inextensional bending) situations, respectively. Locking can be improved by using selective or reduced integration [38, 40]. However, the resulting elements contain spurious zero-energy (hourglass) modes and hence are not reliable [36]. There are several approaches to obtain elements free from locking and spurious modes [44]. In this work, the family of Mixed Interpolation of Tensorial Components (MITC) shell elements [5, 11, 18, 24] developed by Bathe and co-workers is chosen because of its robustness and predictive capability. The approach consists in using covariant strains rather than local or global Cartesian strains, and different interpolation schemes for each strain component. The MITC9 shell element [11] is used in the present paper.

The equilibrium equation of an element e can be written as:

$$\tilde{\mathbf{K}}^{(e)}\mathbf{a}^{(e)} - \mathbf{Q}^{(e)}\mathbf{t}^{(e)} = \mathbf{q}^{(e)} \tag{40}$$

where $\tilde{\mathbf{K}}^{(e)} = \mathbf{K}^{(e)} - \omega^2\mathbf{M}^{(e)}$ is the stiffness matrix for time harmonic analysis, $\mathbf{Q}^{(e)}$ is the distributed mid-surface load matrix and $\mathbf{q}^{(e)}$ is the vector of equilibrating nodal forces and moments. The vector of element Degrees Of Freedom (DOF) $\mathbf{a}^{(e)}$ is composed of vectors of nodal DOF:

$$\mathbf{a}^{(e)} = \begin{pmatrix} \mathbf{a}_1^{(e)} & \dots & \mathbf{a}_p^{(e)} & \dots & \mathbf{a}_N^{(e)} \end{pmatrix}^T \tag{41}$$

where N is the number of nodes of the shell finite element. Each node p has three DOF associated with the displacement of the mid-surface, and two local or three global rotations of the cross-section:

$$\text{5 DOF node:} \quad \mathbf{a}_p^{(e)} = \begin{pmatrix} u_{1p}^{(e)} & u_{2p}^{(e)} & u_{3p}^{(e)} & \alpha_p^{(e)} & \beta_p^{(e)} \end{pmatrix}^T \tag{42}$$

$$\text{6 DOF node:} \quad \mathbf{a}_p^{(e)} = \begin{pmatrix} u_{1p}^{(e)} & u_{2p}^{(e)} & u_{3p}^{(e)} & \theta_{1p}^{(e)} & \theta_{2p}^{(e)} & \theta_{3p}^{(e)} \end{pmatrix}^T \tag{43}$$

For efficiency reasons, nodes with 5 DOF are used by default. Nodes with 6 DOF are used only when strictly required, e.g. folded shells, or when they facilitate the application of boundary conditions, e.g. symmetry conditions. The vector of nodal values of the distributed mid-surface load $\mathbf{t}^{(e)}$ can be written as:

$$\mathbf{t}^{(e)} = \begin{pmatrix} \mathbf{t}_1^{(e)} & \dots & \mathbf{t}_p^{(e)} & \dots & \mathbf{t}_N^{(e)} \end{pmatrix}^T, \mathbf{t}_p^{(e)} = \begin{pmatrix} t_{1p}^{(e)} & t_{2p}^{(e)} & t_{3p}^{(e)} \end{pmatrix}^T \tag{44}$$

where $\mathbf{t}_p^{(e)}$ is expressed in global coordinates.

2.5 BE–FE coupling

The main hypothesis of the presented model over the reality is to assume that the interaction is established between the mid-surface of the shell structure and the soil–shell boundaries idealised as a crack-like boundary. Figure 1 illustrates this hypothesis by using a straight wall buried in a half-space. From the point of view of the soil, the shell structure is geometrically seen as a null thickness inclusion. From the point of view of the shell, the soil interacts on its mid-surface. Therefore, it leads to two approximations:

- Wave diffraction is produced over the mid-surface of the shell structure rather than over its real boundaries, i.e. top-surface, bottom-surface, and edges are ignored. This approximation gets worse as thickness increases, being more pronounced near the shell edges, and also depends on the frequency [8, 41].
- Stiffness and inertia are overestimated by the model if real elastic modulus and densities are used for the shell and the soil. This can be observed on the right part of Figure 1, where the shell region overlaps the soil added when assuming a crack-like boundary. An analogous phenomenon occurs in other soil-structure models, particularly in pile-soil interaction [23, 37]. Some authors propose using corrected properties for the structure ($\tilde{\rho}_{\text{structure}} = \rho_{\text{structure}} - \rho_{\text{soil}}$, $\tilde{E}_{\text{structure}} = E_{\text{structure}} - E_{\text{soil}}$) in order to compensate for them. Except where noted, the examples shown in this paper do not use corrected properties because little differences have been observed for these.

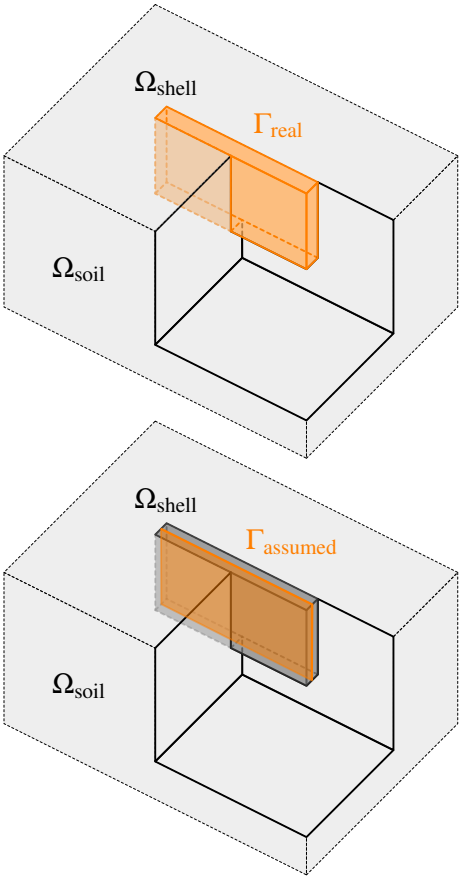

Figure 1: Main hypothesis of the DBEM–FEM model. Top: real interaction between real boundaries. Bottom: assumed interaction between a crack-like boundary in the soil and the mid-surface of the shell.

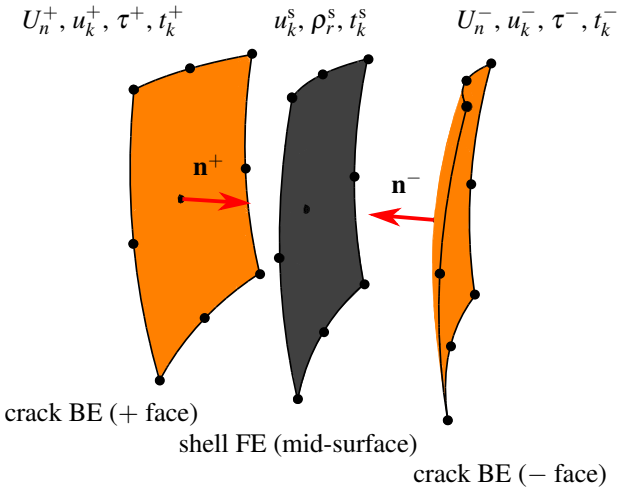

Figure 2: Exploded view of the BE–FE coupling

A direct BE–FE coupling after discretisation is performed, where both crack boundary element mesh and shell finite element mesh must be conforming, see Figure 2. Thus, there are three nodes at a given nodal position: a BE node related to the positive face of the soil, a BE node related to the negative face of the soil, and a FE node related to the shell. Let n_k^+, U_n^+, u_k^+, τ^+ and t_k^+ be respectively the unit normal, fluid normal displacement, solid displacement, fluid equivalent stress and solid traction of the BE node related to the positive face of the soil. Similarly, negative superscripts indicate variables on the negative face. The displacement of the shell mid-surface is denoted as u_k^s, and the distributed mid-surface load as t_k^s. Although other contact conditions may be considered, in the following it is assumed that the shell mid-surface and the soil crack-like boundary are in perfectly welded and impermeable contact. Therefore, compatibility and equilibrium coupling conditions can be written as:

$$\text{Compatibility: } \begin{cases} u_k^+ = u_k^s,\ u_k^- = u_k^s \\ U_n^+ = u_j^s n_j^+,\ U_n^- = u_j^s n_j^- \end{cases} \tag{45}$$

$$\text{Equilibrium: } \tau^+ n_k^+ + t_k^+ + \tau^- n_k^- + t_k^- + t_k^s = 0 \tag{46}$$

These coupling conditions are coherent with the location of all variables involved along the interfaces, except shell rotations, which are not present as degrees of freedom along the soil boundary. It means that there is not a complete displacement coupling because displacement continuity is only guaranteed at nodes. Also, tangential loads acting along the top- and bottom-surfaces of the shell that produce distributed bending moments are completely ignored. Both deficiencies, however, have little significance in most applications. Given that shell structures are almost always stiffer than soils, and the discretisation must be conforming, the size of shell elements are likely to be smaller than required by the elements-per-wavelength criterion, and thus the first deficiency is automatically alleviated. Because of the way most buried shell structures are loaded, the second deficiency is unlikely to be appreciable except for thick shells.

The proposed DBEM–FEM model has several advantages over other purely continuum or mixed continuum -

structural models, which can be grouped into two categories:

Methodological advantages It combines the well known ability of the BEM to deal with wave propagation phenomena in soils with the natural way shell structures are treated by the FEM. Since the shape and thickness of shell finite elements are considered independently, there is no need to define a fully detailed volume geometry. Consequently, the same surface mesh of shell finite elements can be used for studying shell structures of different thicknesses. Likewise, since the soil-shell interface is located at the shell mid-surface due to the use of the DBEM, a surface mesh of crack boundary elements conforming to the shell finite element mesh is all that is needed to model the soil in contact with the structure. Therefore, these simple surface meshes are able to represent the buried open shell structure, being furthermore thickness-independent.

Computational advantages Although it is difficult to quantify the computational advantage of this model because it depends on its implementation and the particular problem at hand, some comparative facts can be given:

- When compared to a multi-region BEM model (see e.g. [27, 28]) using the same element sizes, the number of degrees of freedom per shell node is reduced from 14 to 13 (-7%).
- A reduction in the number of degrees of freedom is automatically achieved since the edges of the shell structure are not discretised, and its thickness does not influence the mesh generation.
- The proposed model avoids common issues related to the BEM when dealing with thin geometries, i.e. quasi-singular integration and bad conditioning issues. Both issues are often alleviated by performing the integrals with a higher number of integration points and/or decreasing the element sizes, consequently increasing computational costs.
- When compared to a conventional multi-region BEM-FEM model applied to open shell structures (see e.g. [25]), there is no need to create fictitious interfaces that produce superfluous degrees of freedom.
- The main disadvantage of this model is the need of a regularised HBIE for the surrounding medium, which has to be obtained, and is computationally costlier than the SBIE. For homogeneous media, this is commonly affordable, but for inhomogeneous (layered, anisotropic, etcetera) media this could be a formidable task.

Regarding the quantification of the computational advantage, a first look is given in Section 3.2, where the proposed DBEM–FEM model and a multi-region BEM model [27, 28] are compared. It is observed that a relevant computation time reduction is achieved mainly due to the decrease of the number of degrees of freedom.

3 Results and discussion

3.1 Validation of the regularised HBIE

In this section, the presented regularised HBIE is validated. For this purpose, the problem of a spherical cavity of radius R_s in a poroelastic full-space and under harmonic radial excitation is considered. This problem has analytical solution, and its curved geometry allows to test all the terms involved in the Boundary Integral Equations.

The analytical solution is obtained by applying the Helmholtz decomposition to the radial displacements after expressing Equations (5) and (6) in spherical coordinates. Taking into account that only outgoing P1 and P2 waves exist in this problem, solid and fluid displacements in the radial direction can be written as:

$$u_r(r) = -\sum_{j=1}^{j=2} D_j \left(ik_{\mathrm{P}j} + \frac{1}{r} \right) \frac{e^{-ik_{\mathrm{P}j}r}}{r} \varphi_{\mathrm{f}j} \tag{47}$$

$$U_r(r) = -\sum_{j=1}^{j=2} \left(ik_{\mathrm{P}j} + \frac{1}{r} \right) \frac{e^{-ik_{\mathrm{P}j}r}}{r} \varphi_{\mathrm{f}j} \tag{48}$$

where $D_j = \varphi_{\mathrm{s}j}/\varphi_{\mathrm{f}j} = -(\omega^2\hat{\rho}_{22} - Rk_{\mathrm{P}j}^2)/(\omega^2\hat{\rho}_{12} - Qk_{\mathrm{P}j}^2)$, and $\varphi_{\mathrm{s}j}$ and $\varphi_{\mathrm{f}j}$ are amplitudes of solid and fluid displacement potentials. Solid stress in the radial direction and fluid equivalent stress can be expressed as:

$$\tau_r(r) = \sum_{j=1}^{j=2} \left[\frac{4\mu D_j}{r} \left(ik_{\mathrm{P}j} + \frac{1}{r} \right) - (D_j\lambda_u + Q)k_{\mathrm{P}j}^2 \right] \frac{e^{-ik_{\mathrm{P}j}r}}{r} \varphi_{\mathrm{f}j} \tag{49}$$

$$\tau(r) = -\sum_{j=1}^{j=2} (QD_j + R)k_{\mathrm{P}j}^2 \frac{e^{-ik_{\mathrm{P}j}r}}{r} \varphi_{\mathrm{f}j} \tag{50}$$

where $\lambda_u = N + \mu$. The amplitudes $\varphi_{\mathrm{f}j}$ are obtained from the linear system of equations formed by the boundary conditions at $r = R_s$. The results presented in this paper correspond to the following two sets of boundary conditions: $\tau_r(R_s) = P$ and $\tau(R_s) = 0$ (permeable cavity), and $\sigma_r(R_s) = \tau_r(R_s) + \tau(R_s) = P$ and $U_r(R_s) = u_r(R_s)$ (impermeable cavity).

The problem is solved for a spherical cavity of radius $R_s = 1$ m, and the following properties of the poroelastic medium (Berea Sandstone [16]): $\rho_{\mathrm{f}} = 1000$ kg/m^3, $\rho_{\mathrm{s}} = 2800$ kg/m^3, $\rho_{\mathrm{a}} = 150$ kg/m^3, $\lambda = 4$ GPa, $\mu = 6$ GPa, $\phi = 0.19$, $R = 0.444$ GPa, $Q = 1.399$ GPa and $b = 0.19 \cdot 10^9$ N$\cdot$s/m^4. In order to present the results in a dimensionless fashion, dimensionless frequency $a_0 = \omega R_s/c_{\mathrm{P}}^u$ is used, where $c_{\mathrm{P}}^u = \sqrt{\lambda_u/(\phi\rho_{\mathrm{f}} + (1-\phi)\rho_{\mathrm{s}})}$ is the undrained P wave propagation speed. Likewise, the quasi-static solid radial displacement $u_r^0 = \lim_{\omega\to 0} u_r$ is used to normalise the displacements.

BEM numerical solutions are obtained by collocating the BIE (SBIE or HBIE) using the MCA with $\delta = 0.23$. Only one-octant of the spherical cavity is discretised, and symmetry conditions with respect to the xy, yz and zx planes are enforced by the classical mirroring approach. Five isoparametric meshes of quadratic triangular elements are considered, including a crude mesh of only 1 element. This is a demanding set of meshes from the point of view of testing the BEM formulation for general curved elements.

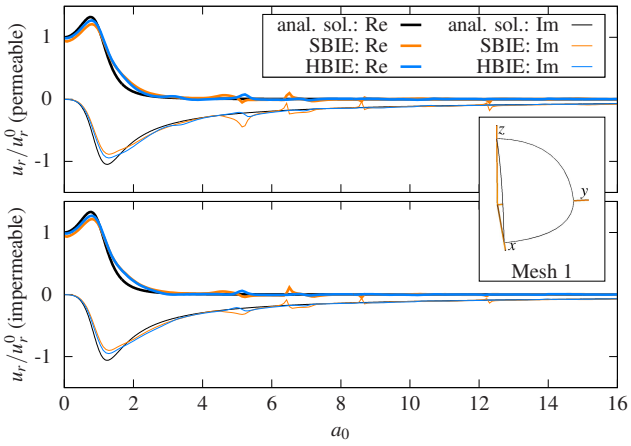

Figure 3: Comparison between analytical and BEM numerical solutions

Mesh	**1**	**2**	**3**	**4**	**5**
N_{elements}	1	4	16	64	256
h [m]	1.41	0.77	0.39	0.20	0.10
E_{G}	2.3E-2	2.2E-3	1.6E-4	1.0E-5	1.2E-6
$\widetilde{E}$ (p, SBIE)	1.3E-1	8.7E-3	2.7E-4	1.1E-5	4.8E-7
$\widetilde{E}$ (p, HBIE)	7.9E-2	7.6E-3	4.0E-4	2.2E-5	1.2E-6
$\widetilde{E}$ (i, SBIE)	1.3E-1	8.5E-3	2.6E-4	1.0E-5	4.4E-7
$\widetilde{E}$ (i, HBIE)	8.1E-2	7.4E-3	3.0E-4	1.2E-5	3.7E-7
eoc_G	N/A	3.73	4.06	4.01	4.03
$\widetilde{eoc}$ (p, SBIE)	N/A	3.76	5.00	4.89	4.48
$\widetilde{eoc}$ (p, HBIE)	N/A	3.63	4.14	4.12	4.23
$\widetilde{eoc}$ (i, SBIE)	N/A	3.76	5.04	4.88	4.53
$\widetilde{eoc}$ (i, HBIE)	N/A	3.66	4.71	4.94	5.09

Table 1: Convergence of the BEM numerical solution for permeable (p) and impermeable (i) boundary conditions.

Since the solution is one-dimensional in the radial direction, i.e. radial displacements and stresses are constant over the cavity's surface, numerical errors are mainly due to the geometric discretisation error. The average geometric discretisation error E_{G} for a spherical surface can be defined as:

$$E_{\text{G}} = \frac{\int_{A_{\text{mesh}}} |\mathbf{x}_{\text{mesh}} - \mathbf{x}_{\text{surface}}| / R_s \, \mathrm{d}A}{\pi R_s^2 / 2} \tag{51}$$

where $\mathbf{x}_{\text{surface}}$ is the nearest point of the spherical surface to a point of the mesh $\mathbf{x}_{\text{mesh}}$.

Figure 3 shows analytical and BEM numerical solutions using the crude mesh, for the frequency range $a_0 = (0, 16]$ and both sets of boundary conditions. Figures 4 and 5 show BEM numerical errors and orders of convergence . BEM numerical results are shown as average absolute errors:

$$E = \frac{\int_{A_{\text{mesh}}} |u_r^{(\text{numerical})} - u_r| / |u_r^0| \, \mathrm{d}A}{\pi R_s^2 / 2} \tag{52}$$

The experimental order of convergence eoc between results obtained from two different meshes i and j is defined as:

$$eoc = \log(E^{(i)}/E^{(j)}) / \log(h^{(i)}/h^{(j)}) \tag{53}$$

where h denotes element size, and mesh j is finer than i. Table 1 shows a summary of mesh data and results, where

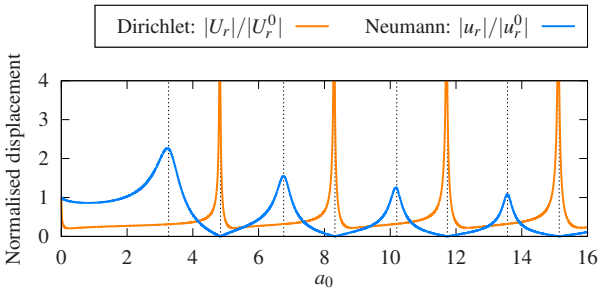

Figure 6: Analytical solution of a sphere with Dirichlet B.C. ($\tau_r(R_s) = 0$, $u_r(R_s) = U$) and Neumann B.C. ($U_r(R_s) = U$, $\tau_r(R_s) = 0$)

frequency-averaged errors and experimental orders of convergence are denoted respectively as $\widetilde{E}$ and $\widetilde{eoc}$. These averaged values are computed from the frequency range $(0, \pi/h]$, i.e. the range where there are at least two elements per wavelength.

Results show that the SBIE and the HBIE behave hand in hand regarding the error levels for all meshes and frequencies. Convergence of the BEM using both the SBIE and the HBIE is demonstrated since E reduces in the same way as E_{G} does for each mesh, and within the whole frequency range. The expected order of convergence for quadratic elements is 3. However, the observed eoc within the relevant frequency range varies around 4, being very similar to the order of convergence of the geometric discretisation eoc_{G}. When observing the obtained experimental orders of convergence, it is possible to distinguish three zones within the frequency range. For frequencies where there are less than two elements per wavelength, eoc is highly oscillatory. For frequencies where there are between two and approximately four elements per wavelength, eoc is higher than expected. And finally, for frequencies where there are more than approximately four elements per wavelength, eoc smoothly varies around eoc_{G}.

Regarding the BEM numerical errors, several peaks are observed at different frequencies for the SBIE and HBIE. They are related to the ill-conditioning of the exterior problem (spherical cavity) near the natural frequencies of an interior problem (sphere), see e.g. [13]. These natural frequencies correspond to the sphere with Dirichlet boundary conditions ($\tau_r(R_s)$ and $u_r(R_s)$ prescribed) for the spherical cavity solved using the SBIE, and to the sphere with Neumann boundary conditions ($U_r(R_s)$ and $\tau_r(R_s)$ prescribed) for the spherical cavity solved using the HBIE. Figure 6 shows the analytical solution of the Dirichlet and Neumann interior problems, and the observed natural frequencies are indicated by vertical dashed lines. For comparison purposes, they are also indicated in the bottom error graphs in Figures 4 and 5.

3.2 Application to a wave diffraction problem

In this section, the presented DBEM–FEM dynamic model is used in a wave diffraction problem, and compared against a multi-region BEM model [27, 28]. A curved vibration isolation wall buried in a poroelastic half-space under a

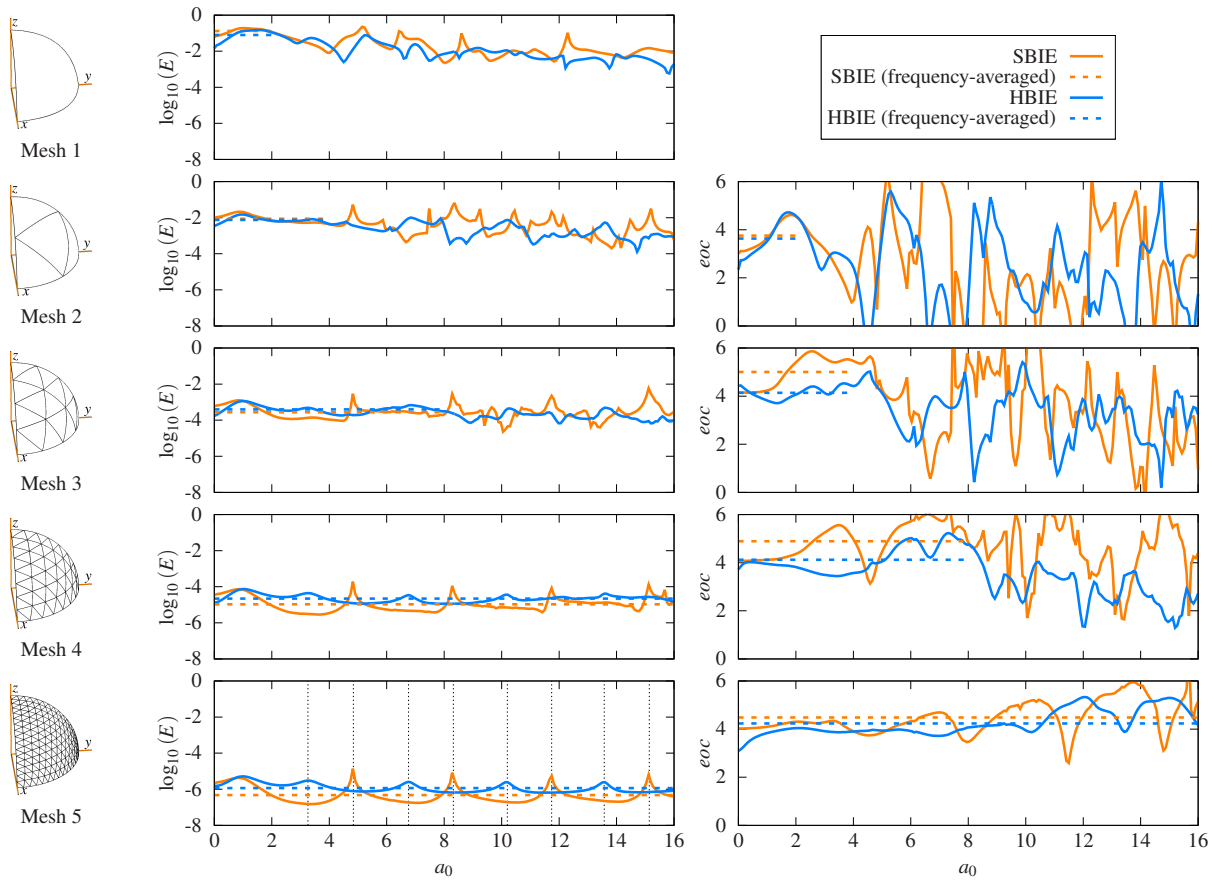

Figure 4: Validation of the regularised HBIE. Spherical cavity with $\tau_r(R_s) = P$ and $\tau(R_s) = 0$ (permeable).

Rayleigh wave field is considered. The wall has a radius of 6 m, a depth of $H = 4$ m, covers an angle of 90°, and different thicknesses $t = \{0.80, 0.40, 0.08, 0.04\}$ m are studied. Thus, slendernesses ranging from $H/t = 5$ to $H/t = 100$ are analysed. The wall is considered to be made of concrete with density $\rho = 2400\,\mathrm{kg/m^3}$, shear modulus $\mu = 6.5$ GPa, Poisson's ratio $\nu = 0.15$, and hysteretic damping ratio $\xi = 0.05$, where the complex shear modulus used is $\mu^* = (1 + i2\xi)\mu$. The poroelastic half-space has the following properties taken from Kassir et al. [22]: $\rho_\mathrm{f} = 1000\,\mathrm{kg/m^3}$, $\rho_\mathrm{s} = 1425\,\mathrm{kg/m^3}$, $\lambda = \mu = 32.18$ MPa, $\phi = 0.35$, $\rho_\mathrm{a} = 0\,\mathrm{kg/m^3}$, $R = 248$ MPa, $Q = 461$ MPa, $b = 1.1986 \cdot 10^7\,\mathrm{N \cdot s/m^4}$; and the free-surface is permeable, i.e. $\tau = t_k = 0$ at $z = 0$. As a source of vibrations, an incident Rayleigh wave field [9] with unitary vertical displacements is impinging along the x-axis at $f = 50$ Hz. Since the zx-plane is a symmetry plane, only one-half of the domain is discretised and appropriate symmetry conditions are thus enforced.

Figure 7 shows an example of multi-region BEM and DBEM–FEM meshes, where it can be observed the simplicity of the latter. At the wall, there are two conforming meshes in the DBEM–FEM model: a BE mesh with crack boundary elements representing the soil-wall interface, and a FE mesh with shell finite elements representing the wall. For each thickness, the multi-region BEM model requires a new discretisation, while the DBEM-FEM model only requires changing the shell thicknesses. The multi-region BEM model requires some control of the element size with respect to the thickness in order to avoid integration and conditioning problems. Also, due to the presence of the geometrical details of the wall, more degrees of freedom are required for the wall edges and the free-surface near the wall, especially for small thicknesses. Since the DBEM–FEM model does not require different meshes for different wall thicknesses, they can be changed without needing to build the whole linear system of equations for each case, but only the stiffness and mass matrices.

Figures 8 and 9 show respectively far-field and near-field results for all thicknesses, which are arranged in columns. Figure 8 shows Amplitude Reduction ratios in x and z directions ($AR_j = \mathrm{abs}(u_j/u_j^{\mathrm{incident}})$) along the x-axis for $y = z = 0$. Figure 9 shows displacements, fluid equivalent stress and tractions along the depth of the outer face of the wall, i.e. along the z-axis for $y = 0$ and $x = t/2$ (multi-region BEM) and $x = 0^+$ (DBEM–FEM).

Multi-region BEM meshes are similar to that shown in Figure 7, where a mesh of 11×11, 8×8, 8×8 and 8×8 nine-node quadrilateral boundary elements are used for the faces of the wall with respectively $t = 0.04$, 0.08, 0.4 and 0.8 m. The criteria to mesh the wall and its surroundings have been: a) at least six elements per wavelength, and b) elements of lengths up to ten times the wall thickness. Two DBEM–FEM meshes are considered: (1) soil and wall discretised with a mesh of 8×8 nine-node quadrilateral crack boundary elements and MITC9 shell finite elements, and (2) with a coarse mesh of only 4×4 elements.

Results show the convergence of the DBEM-FEM model

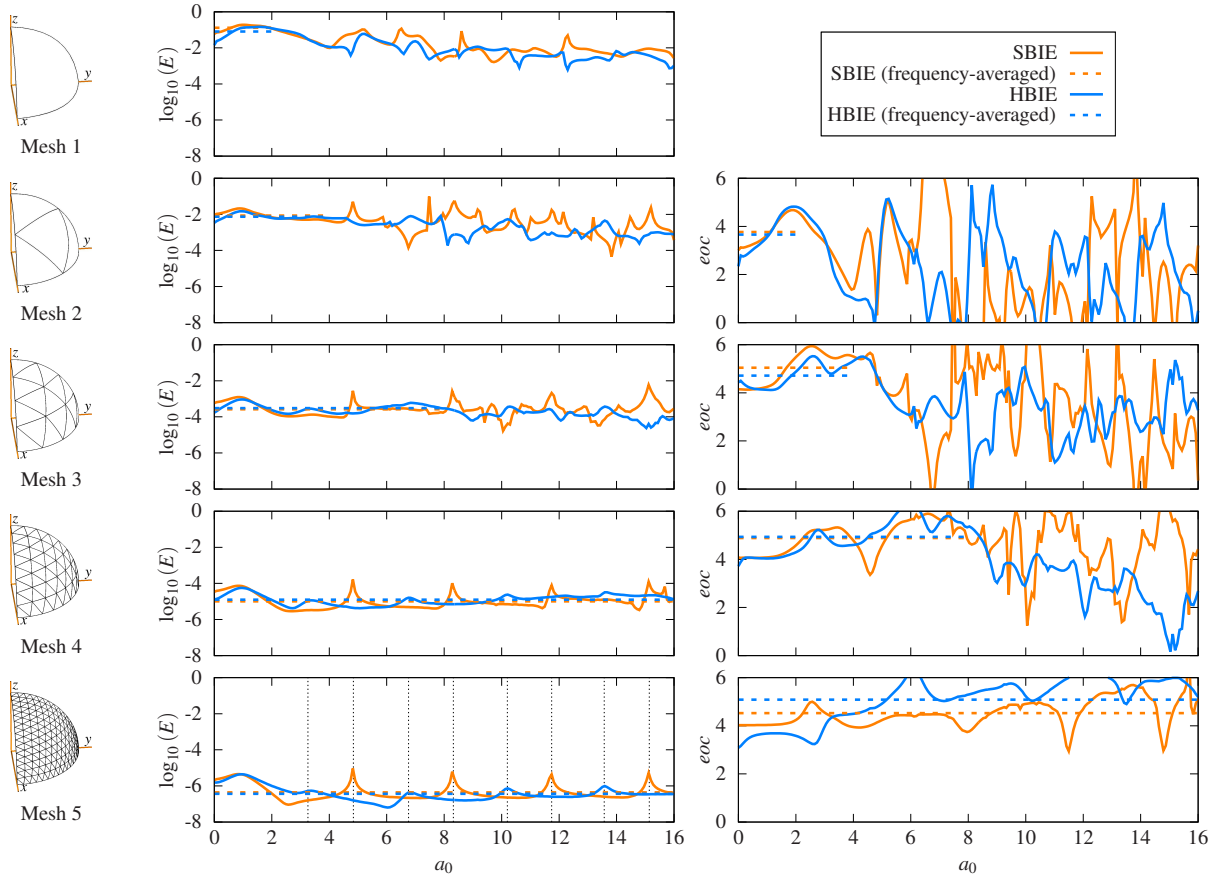

Figure 5: Validation of the regularised HBIE. Spherical cavity with $\sigma_r(R_s) = \tau_r(R_s) + \tau(R_s) = P$ and $U_r(R_s) = u_r(R_s)$ (impermeable).

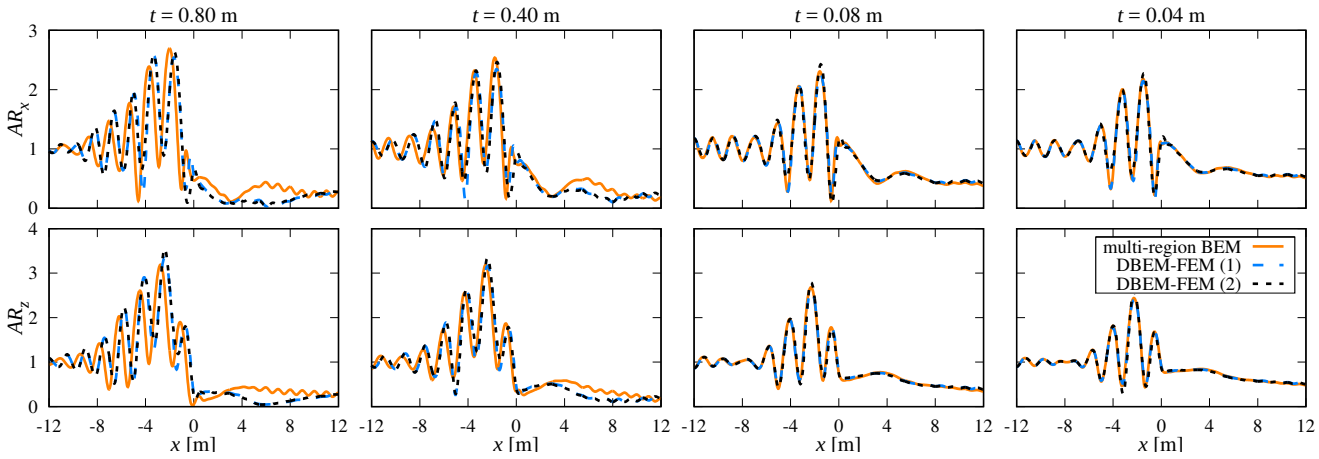

Figure 8: Amplitude Reduction of horizontal (AR_x) and vertical (AR_z) solid displacements along the free-surface at $y = z = 0$. Rayleigh incident wave with unitary vertical displacements at $f = 50$ Hz.

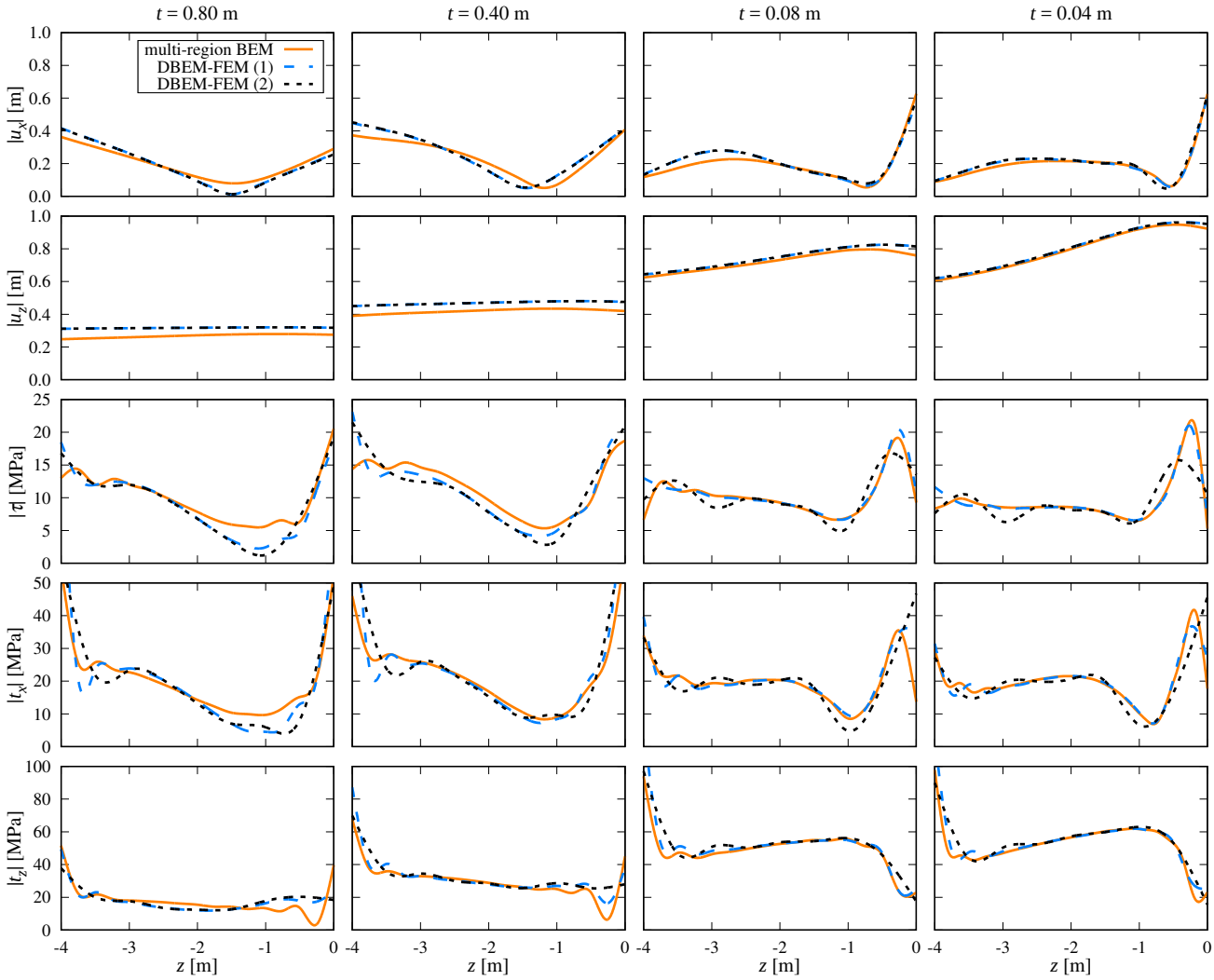

Figure 9: Displacements u_x and u_z, fluid equivalent stress τ, and solid tractions t_x and t_z along the outer face of the wall. Rayleigh incident wave with unitary vertical displacements at $f = 50$ Hz.

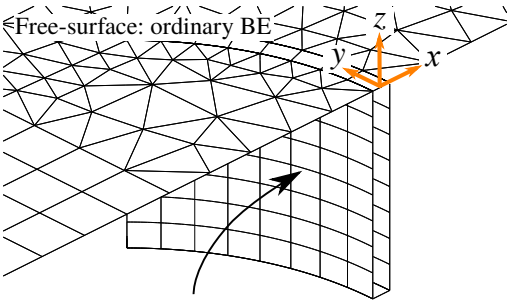

Soil - wall: coupled ordinary BE - BE

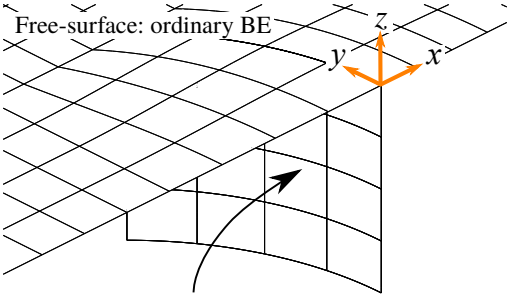

Soil - wall: coupled crack BE - shell FE

Figure 7: Application to a wave diffraction problem (vibration isolation wall). Top: multi-region BEM example mesh. Bottom: DBEM-FEM example mesh.

Mesh	N_{DOF}	t_{build} [s]	t_{solve} [s]	t_{total} [s]
BEM / $t = 0.04$ m	39851	207	175	382
BEM / $t = 0.08$ m	35729	175	128	303
BEM / $t = 0.40$ m	34177	158	113	271
BEM / $t = 0.80$ m	34161	158	112	270
DBEM–FEM (1)	32935	151	101	252
DBEM–FEM (2)	29623	125	75	200

Table 2: Computation times for solving the wave diffraction problem

when $H/t \to \infty$, having excellent agreement for slendernesses $H/t \geq 10$. Nevertheless, the DBEM–FEM model is able to roughly capture the response even for the case of slenderness $H/t = 5$. Results regarding Amplitude Reduction ratios clearly show that in the DBEM–FEM model interaction is happening on the wall mid-surface rather than on the real boundaries of the wall. It is able to reproduce the displacement field, although with a spatial shift that depends on the thickness of the shell structure. This approximation may or may not be acceptable depending on the application at hand. Results along the outer face of the wall demonstrate that even near-field results are in good agreement with those of the multi-region BEM model. Differences are mainly found near the edges, although these become appreciable only for the smaller slendernesses. Coarse DBEM-FEM mesh (2) gives almost identical results than the fine DBEM-FEM mesh (1) regarding results along the free-surface. However, there are small differences on the fluid equivalent stress and solid tractions along the wall, being appreciable near the edges for the smaller slendernesses.

Table 2 shows computation times when solving the problem for each wall thickness and mesh using a 28×2.6 GHz workstation. Computation times for DBEM–FEM meshes

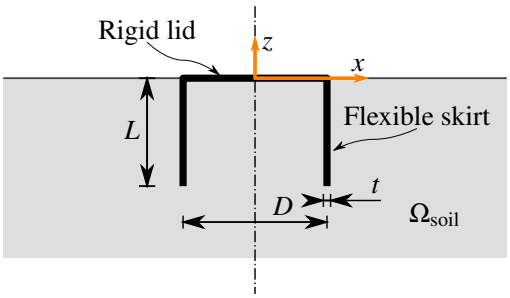

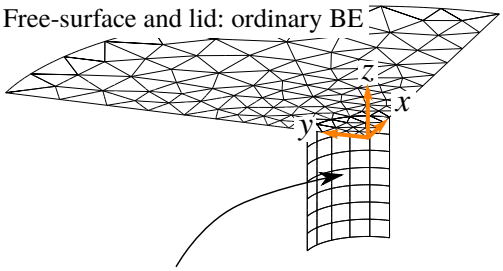

Soil - skirt: crack BE - shell FE

Figure 10: Bucket foundation. Top: layout of the problem. Bottom: DBEM–FEM example mesh.

correspond to the solution of the problem for one individual thickness. Despite the additional costs of evaluating the HBIE, the building time of DBEM–FEM models is only moderately affected when comparing multi-region BEM and DBEM–FEM meshes. More important is the fact that the DBEM–FEM intrinsically leads to a considerable reduction of the number of degrees of freedom, which is what greatly decrease the total computation time. This is clearly more advantageous as the wall thickness reduces, where the approximation introduced by the DBEM–FEM model is also less relevant.

3.3 Application to the evaluation of bucket foundation dynamic stiffnesses

In this section, the present approach is used for the calculation of impedances of bucket foundations in poroelastic soils in order to see the transition from drained to undrained conditions. Impedances of flexible bucket foundations in elastic soils have been studied by Liingaard et al. [25]. This type of foundation has two main parts: the lid, which is a stiffened circular steel plate in contact with the mudline, and the skirt, which is a cylindrical steel shell buried into the seabed soil. Due to the stiffening, the lid can be considered rigid for the present analysis. Therefore, the geometry is defined by the bucket diameter D (or radius R), the skirt length L, and the skirt thickness t. It is assumed that the bucket is installed in a poroelastic half-space, with perfectly bonded (non-relaxed) interface conditions, and it is considered massless. Figure 10 depicts the layout of the problem and an example mesh, including the considered coordinate reference system. As in the previous problem, symmetry properties of the problem are exploited and only a quarter of the domain is discretised.

The impedances are calculated with respect to the dis-

placements and rotations at the centre of the rigid lid. In order to obtain them, unitary displacement and rotations are given to the lid, and then resultant forces and moments are evaluated. Given that the foundation is axisymmetric, the 6 DOF impedance matrix $\mathbf{S}$ is composed of 5 different impedances [25]: swaying S_{HH}, vertical S_{VV}, rocking S_{MM}, rocking - swaying coupling S_{MH}, and torsional S_{TT}; which can be arranged in a dimensionless fashion as follows:

$$\begin{Bmatrix} F_1/\mu R^2 \\ F_2/\mu R^2 \\ F_3/\mu R^2 \\ M_1/\mu R^3 \\ M_2/\mu R^3 \\ M_3/\mu R^3 \end{Bmatrix} = \begin{bmatrix} S_{HH} & 0 & 0 & 0 & S_{MH} & 0 \\ 0 & S_{HH} & 0 & -S_{MH} & 0 & 0 \\ 0 & 0 & S_{VV} & 0 & 0 & 0 \\ 0 & -S_{MH} & 0 & S_{MM} & 0 & 0 \\ S_{MH} & 0 & 0 & 0 & S_{MM} & 0 \\ 0 & 0 & 0 & 0 & 0 & S_{TT} \end{bmatrix} \begin{Bmatrix} u_1/R \\ u_2/R \\ u_3/R \\ \theta_1 \\ \theta_2 \\ \theta_3 \end{Bmatrix} \tag{54}$$

Figure 11 shows the absolute values of these impedances for bucket foundations of different L/D ratios buried in sandy soils with different hydraulic conductivities. The bucket has a diameter $D = 10$ m, and the considered L/D ratios range from 0 (bucket without skirt), 0.5, 1 and 2. The skirt has a thickness of 5 cm. The bucket is made of steel with Young's modulus $E = 210$ GPa, Poisson's ratio $\nu = 0.25$ and hysteretic damping ratio $\xi = 0.01$, where the complex Young's modulus used is $E^* = (1 + i2\xi)E$. The properties of the sand are taken from the work from Buchanan and Gilbert [12], where it is called "fine sand": frame shear modulus $\mu^* = 7.12 + i0.23$ MPa, frame bulk modulus $K^* = 9.49 + i0.30$ MPa, Poisson's ratio $\nu = 0.20$, porosity $\phi = 0.43$, fluid bulk modulus $K_\mathrm{f} = 2.39$ GPa, Biot's coupling parameters $Q = 1.362$ GPa and $R = 1.028$ GPa, fluid density $\rho_\mathrm{f} = 1000$ kg/m^3, fluid density $\rho_\mathrm{s} = 2670$ kg/m^3, additional apparent density $\rho_\mathrm{a} = 107.5$ kg/m^3, and fluid viscosity $\eta = 1.01$ mPa$\cdot$s. According to Lin et al. [26], for a fine sand and within the area where Biot's theory is applicable, the hydraulic conductivity k can range between 10^{-2} and 10^{-6} m/s. Therefore, five different hydraulic conductivities ranging from drained, partially drained and undrained soils are considered: $k \to \infty$ (drained elastic soil), $k = 10^{-2}$, $k = 10^{-4}$, $k = 10^{-6}$, and $k \to 0$ (undrained elastic soil) m/s. A dimensionless frequency $a_0 = \omega R/c_\mathrm{S}^\mathrm{u}$ is used, where $c_\mathrm{S}^\mathrm{u} = \sqrt{\mu/(\phi\rho_\mathrm{f} + (1-\phi)\rho_\mathrm{s})}$ is the undrained S wave velocity. The frequency range and scaling shown in Figure 11 has been chosen so that the transition from drained to undrained conditions can be clearly seen for each impedance and bucket geometry.

It is well known that for $a_0 \to 0$ the response using a poroelastic model with finite hydraulic conductivity k tends to a drained elastic soil, while for $a_0 \to \infty$ the response of a poroelastic model tends to the undrained elastic soil. However, the difference between impedances under drained and undrained conditions, and the location where the transition takes place in the frequency domain, depends on several factors.

The most important factor influencing the difference between impedances under drained and undrained conditions is the presence of P waves. Due to the bucket geometry and the absence of P waves in the torsional mode, the torsional impedance shown in Figure 11 does not depend on hydraulic conductivity, and any poroelastic soil behaves as the undrained elastic one. All other impedances imply P waves and hence are sensitive to hydraulic conductivity, although their origin and relevance are different. In the vertical mode, P waves are mostly originated from the lid, and thus, for a given diameter D, the difference between drained and undrained impedances does not depend on the length L nor L/D ratio. However, in relative terms, this difference is more important for small L/D ratios because the impedance values are smaller. In the swaying mode, P waves are mainly originated from the skirt, and then the difference between drained and undrained impedances does depend on both diameter D and length L. In relative terms, however, these differences are equally significant for different L/D ratios because they increase as the impedance values increase. The rocking mode produces P waves from the lid and the bucket, and hence both diameter D and length L influence the difference between drained and undrained impedances. The difference of impedances measured in relative terms is considerable for all L/D ratios studied, being more important for smaller L/D ratios. Rocking-swaying impedances have significant differences between completely drained and undrained impedances. They are approximately constant in relative terms for all L/D ratios, except for the case $L/D = 0$ of a bucket without skirt (circular footing). The influence of this coupling impedance in the impedance matrix is negligible for very small L/D ratios because its magnitude is much smaller than swaying and rocking impedances, but as L/D increases the coupling impedance becomes appreciable.

For all impedances except the rocking impedance, soils are virtually behaving in undrained conditions for dimensionless frequencies $a_0 > 1$, i.e. $f > 2$ Hz for the considered soil. For the rocking impedance, soils start behaving in undrained conditions at higher frequencies, especially for small L/D ratios. As expected, the drained to undrained transition frequency decreases as the hydraulic conductivity decreases.

This type of foundations is now very important because of its potential as foundations of Offshore Wind Turbines. The range of frequencies of interest depends on the type of analysis, the site environmental conditions and the wind turbine [2]. For dynamic loading analysis, one could take a range from about 0.05 Hz to a few Hertz typically. This corresponds to dimensionless frequencies greater than $a_0 = 10^{-2}$ for the soil properties used in this example. It can be seen in Figure 11 that, for hydraulic conductivities greater than 10^{-4} m/s, the drained/undrained transition takes place within the range of frequencies of interest. The importance of this fact depends on multiple factors: soil properties, foundation design, wind turbine, etc.; but it should certainly be taken into account.

4 Conclusions

In this paper, a three-dimensional boundary element – finite element dynamic model of open shells surrounded by a poroelastic medium is presented. It uses the Dual BEM for the surrounding medium, which is a Biot poroelastic medium, and MITC shell elements for the shell structure.

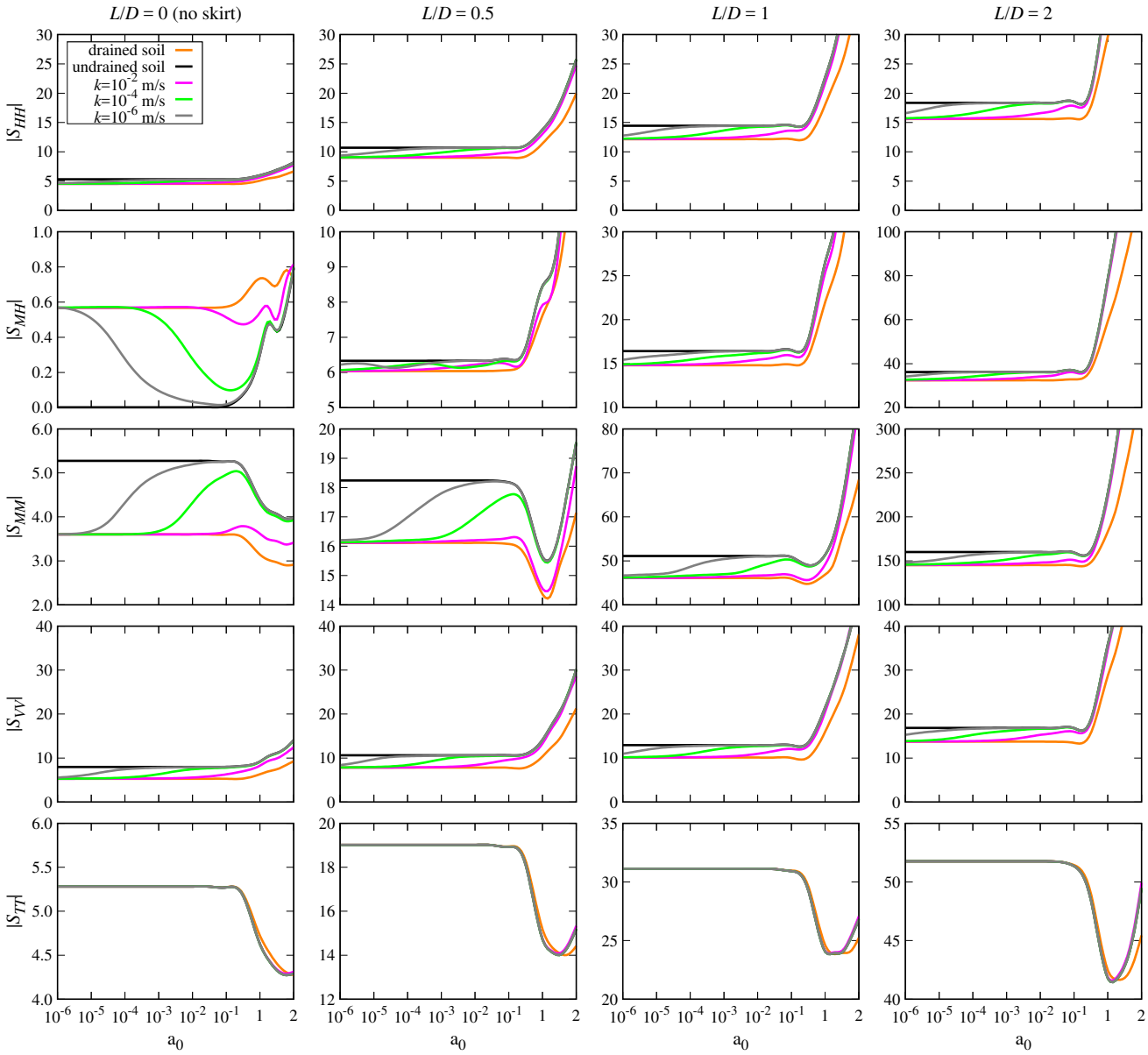

Figure 11: Impedances (absolute value) of bucket foundations of different L/D ratios installed in sandy soils

For this purpose, an analytically regularised HBIE needed for the Dual BEM has been obtained.

The analytically regularised HBIE has been validated using the problem of a spherical cavity under radial excitation. The DBEM–FEM model has been used in a wave diffraction problem in order to show its efficacy. It has been shown that it is accurate enough for moderately thin structures, i.e. slendernesses greater than 10, and relatively coarse meshes. It has also been used to calculate the impedances of bucket foundations in a sandy soil with different hydraulic conductivities. It has been observed that all impedances except the torsional one have appreciable sensitivity to hydraulic conductivity. Taking into account that bucket foundations are being studied as foundation solutions for Offshore Wind Turbines, it has been found that this sensitivity may be relevant for their dynamic analysis.

acknowledgements

We would like to recognise and thank Professor Fernando Medina (Universidad de Sevilla) for contributing with many ideas behind this work, which emerged in meetings during Spring 2012.

This work was supported by the Subdirección General de Proyectos de Investigación of the Ministerio de Economía y Competitividad (MINECO) of Spain and FEDER through Research Project BIA2014-57640-R. J.D.R. Bordón is recipient of the research fellowship FPU13-01224 from the Ministerio de Educación, Cultura y Deportes (MECD) of Spain. The authors are grateful for this support.

`Gmsh` has been used as mesh generator, pre- and post-processing utility [20] in this paper. We would like to appreciate the effort of this team in providing this software to the community.

Finally, the authors wish to thank the Reviewers for their comments, which have improved the manuscript.

A Description of matrices $\mathbf{I}^{\mathrm{i}}_{\mathrm{S}}$, $\mathbf{I}^{\mathrm{i}}_{\mathrm{H}}$, $\mathbf{U}^*$, $\mathbf{T}^*$, $\mathbf{D}^*$ and $\mathbf{S}^*$

Let $\mathbf{x}$ and $\mathbf{n}$ be the position and unit normal vectors of the observation point, while $\mathbf{x}^{\mathrm{i}}$ and $\mathbf{n}^{\mathrm{i}}$ are those of the collocation point. The distance vector between both points is $\mathbf{r} = \mathbf{x} - \mathbf{x}^{\mathrm{i}}$, its norm is $r = |\mathbf{r}|$, and the distance derivative is denoted as $r_{,j} = \partial r / \partial x_j$. The partial derivatives of the distance with respect to the unit normal vectors are $\partial r/\partial n = r_j n_j$ and $\partial r/\partial n^{\mathrm{i}} = -r_j n^{\mathrm{i}}_j$. For the sake of brevity, the wavenumbers are rewritten as $k_j = k_{\mathrm{P}j}$ and $k_3 = k_{\mathrm{S}}$, and the following frequency-dependent parameters are defined:

$$J = \frac{1}{\hat{\rho}_{22}\omega^2},\ Z = \frac{\hat{\rho}_{12}}{\hat{\rho}_{22}},\ \alpha_j = k_j^2 - \frac{\mu}{\lambda+2\mu}k_3^2,\ \beta_j = \frac{\mu}{\lambda+2\mu}k_j^2 - \frac{k_j^2 k_3^2}{k_3^2} \tag{A.1}$$

The matrices $\mathbf{I}^{\mathrm{i}}_{\mathrm{S}}$ and $\mathbf{I}^{\mathrm{i}}_{\mathrm{H}}$ appearing respectively in SBIE and HBIE are:

$$\mathbf{I}^{\mathrm{i}}_{\mathrm{S}} = \begin{bmatrix} J & 0 \\ 0 & \delta_{lk} \end{bmatrix},\ \mathbf{I}^{\mathrm{i}}_{\mathrm{H}} = \begin{bmatrix} 1 & 0 \\ 0 & \delta_{lk} \end{bmatrix} \tag{A.2}$$

The fundamental solution matrix $\mathbf{U}^*$ is:

$$\mathbf{U}^* = \begin{bmatrix} -\tau^*_{00} & u^*_{0k} \\ -\tau^*_{l0} & u^*_{lk} \end{bmatrix} \tag{A.3}$$

where:

$$\tau^*_{00} = \frac{1}{4\pi}\eta \tag{A.4}$$

$$\eta = \frac{1}{k_1^2 - k_2^2}\left[\frac{\alpha_1}{r}e^{-ik_1 r} - \frac{\alpha_2}{r}e^{-ik_2 r}\right] \tag{A.5}$$

$$u^*_{0k} = -\frac{1}{4\pi}\Theta r_{,k} \tag{A.6}$$

$$\Theta = \frac{Q/R - Z}{\lambda+2\mu}\frac{1}{k_1^2-k_2^2}\left[\left(\frac{1}{r^2}+\frac{ik_1}{r}\right)e^{-ik_1 r} - \left(\frac{1}{r^2}+\frac{ik_2}{r}\right)e^{-ik_2 r}\right] \tag{A.7}$$

$$\tau^*_{l0} = \frac{1}{4\pi J}\Theta r_{,l} \tag{A.8}$$

$$u^*_{lk} = \frac{1}{4\pi\mu}\left(\delta_{lk}\psi - \chi r_{,l} r_{,k}\right) \tag{A.9}$$

$$\psi = \frac{1}{r}e^{-ik_3 r} + \frac{1}{r}\left(\frac{1}{ik_3 r} + \frac{1}{(ik_3 r)^2}\right)e^{-ik_3 r} - \frac{1}{k_1^2-k_2^2}\cdot \left[\frac{\beta_1}{r}\left(\frac{1}{ik_1 r}+\frac{1}{(ik_1 r)^2}\right)e^{-ik_1 r} - \frac{\beta_2}{r}\left(\frac{1}{ik_2 r}+\frac{1}{(ik_2 r)^2}\right)e^{-ik_2 r}\right] \tag{A.10}$$

$$\chi = \frac{1}{r}\left(1 + \frac{3}{ik_3 r} + \frac{3}{(ik_3 r)^2}\right)e^{-ik_3 r} - \frac{1}{k_1^2-k_2^2}\cdot \left[\frac{\beta_1}{r}\left(1+\frac{3}{ik_1 r}+\frac{3}{(ik_1 r)^2}\right)e^{-ik_1 r} - \frac{\beta_2}{r}\left(1+\frac{3}{ik_2 r}+\frac{3}{(ik_2 r)^2}\right)e^{-ik_2 r}\right] \tag{A.11}$$

The fundamental solution matrix $\mathbf{T}^*$ is:

$$\mathbf{T}^* = \begin{bmatrix} -(U^*_{n00} + JX'^*_j n_j) & t^*_{0k} \\ -U^*_{nl0} & t^*_{lk} \end{bmatrix} \tag{A.12}$$

where:

$$U^*_{n00} + JX'^*_j n_j = \frac{1}{4\pi}W_0\frac{\partial r}{\partial n} \tag{A.13}$$

$$W_0 = Z\Theta - J\frac{\partial \eta}{\partial r} \tag{A.14}$$

$$t^*_{0k} = \frac{1}{4\pi}\left[T_{01} r_{,k}\frac{\partial r}{\partial n} + T_{02} n_k\right] \tag{A.15}$$

$$T_{01} = -2\mu\left(\frac{\partial \Theta}{\partial r} - \frac{1}{r}\Theta\right) \tag{A.16}$$

$$T_{02} = -\lambda\left(\frac{\partial \Theta}{\partial r} + \frac{2}{r}\Theta\right) - 2\mu\frac{1}{r}\Theta + \frac{Q}{R}\eta \tag{A.17}$$

$$U^*_{nl0} = \frac{1}{4\pi\mu}\left[W_1 r_{,l}\frac{\partial r}{\partial n} + W_2 n_l\right] \tag{A.18}$$

$$W_1 = Z\chi - \mu\left(\frac{\partial \Theta}{\partial r} - \frac{1}{r}\Theta\right) \tag{A.19}$$

$$W_2 = -Z\psi - \mu\frac{1}{r}\Theta \tag{A.20}$$

$$t^*_{lk} = \frac{1}{4\pi}\left[T_1 r_{,l} r_{,k}\frac{\partial r}{\partial n} + T_2\left(\delta_{lk}\frac{\partial r}{\partial n} + r_{,k} n_l\right) + T_3 r_{,l} n_k\right] \tag{A.21}$$

$$T_1 = -2\left(\frac{\partial \chi}{\partial r} - \frac{2}{r}\chi\right) \tag{A.22}$$

$$T_2 = \frac{\partial \psi}{\partial r} - \frac{1}{r}\chi \tag{A.23}$$

$$T_3 = -\frac{2}{r}\chi + \frac{\lambda}{\mu}\left(\frac{\partial \psi}{\partial r} - \frac{\partial \chi}{\partial r} - \frac{2}{r}\chi\right) + \frac{Q}{R}\frac{1}{J}\Theta \tag{A.24}$$

The fundamental solution matrix $\mathbf{D}^*$ is:

$$\mathbf{D}^* = \begin{bmatrix} -d^*_{00} & d^*_{0k} \\ -d^*_{l0} & d^*_{lk} \end{bmatrix} \tag{A.25}$$

where:

$$d^*_{00} = \frac{1}{4\pi J}W_0\frac{\partial r}{\partial n^{\mathrm{i}}} \tag{A.26}$$

$$d^*_{0k} = \frac{1}{4\pi\mu}\left(-W_1 r_{,k}\frac{\partial r}{\partial n^{\mathrm{i}}} + W_2 n^{\mathrm{i}}_k\right) \tag{A.27}$$

$$d^*_{l0} = \frac{1}{4\pi J}\left(-T_{01} r_{,l}\frac{\partial r}{\partial n^{\mathrm{i}}} + T_{02} n^{\mathrm{i}}_l\right) \tag{A.28}$$

$$d^*_{lk} = \frac{1}{4\pi}\left[T_1 r_{,l} r_{,k}\frac{\partial r}{\partial n^{\mathrm{i}}} - T_2\left(-\delta_{lk}\frac{\partial r}{\partial n^{\mathrm{i}}} + r_{,l} n^{\mathrm{i}}_k\right) - T_3 r_{,k} n^{\mathrm{i}}_l\right] \tag{A.29}$$

The fundamental solution matrix $\mathbf{S}^*$ is:

$$\mathbf{S}^* = \begin{bmatrix} -s^*_{00} & s^*_{0k} \\ -s^*_{l0} & s^*_{lk} \end{bmatrix} \tag{A.30}$$

where:

$$s^*_{00} = \frac{1}{4\pi}\left[Q_1\frac{\partial r}{\partial n}\frac{\partial r}{\partial n^{\mathrm{i}}} + Q_2\left(\mathbf{n}\cdot\mathbf{n}^{\mathrm{i}}\right)\right] \tag{A.31}$$

$$Q_1 = \frac{Z^2}{\mu}\chi - 2Z\left(\frac{\partial \Theta}{\partial r} - \frac{1}{r}\Theta\right) + J\left(\frac{\partial^2 \eta}{\partial r^2} - \frac{1}{r}\frac{\partial \eta}{\partial r}\right) \tag{A.32}$$

$$Q_2 = \frac{Z^2}{\mu}\psi + 2Z\frac{1}{r}\Theta - J\frac{1}{r}\frac{\partial \eta}{\partial r} \tag{A.33}$$

$$s^*_{0k} = \frac{1}{4\pi}\left\{ S_{01} r_{,k} \frac{\partial r}{\partial n}\frac{\partial r}{\partial n^{\mathrm{i}}} + S_{02} n_k \frac{\partial r}{\partial n^{\mathrm{i}}} + S_{03}\left[n^{\mathrm{i}}_k \frac{\partial r}{\partial n} + r_{,k}\left(\mathbf{n}\cdot\mathbf{n}^{\mathrm{i}}\right)\right]\right\} \tag{A.34}$$

$$S_{01} = -2Z\left(\frac{\partial \chi}{\partial r} - \frac{2}{r}\chi\right) - 2\mu\left[-\frac{\partial^2 \Theta}{\partial r^2} + \frac{3}{r}\left(\frac{\partial \Theta}{\partial r} - \frac{1}{r}\Theta\right)\right] \tag{A.35}$$

$$S_{02} = \frac{Q}{R}\left(\frac{Z}{J}\Theta - \frac{\partial \eta}{\partial r}\right) + Z\left[\frac{\lambda}{\mu}\left(\frac{\partial \psi}{\partial r} - \frac{\partial \chi}{\partial r} - \frac{2}{r}\chi\right) - \frac{2}{r}\chi\right] + \lambda\left[\frac{\partial^2 \Theta}{\partial r^2} + \frac{2}{r}\left(\frac{\partial \Theta}{\partial r} - \frac{1}{r}\Theta\right)\right] + 2\mu\frac{1}{r}\left(\frac{\partial \Theta}{\partial r} - \frac{1}{r}\Theta\right) \tag{A.36}$$

$$S_{03} = -Z\left(\frac{\partial \psi}{\partial r} - \frac{1}{r}\chi\right) - 2\mu\frac{1}{r}\left(\frac{\partial \Theta}{\partial r} - \frac{1}{r}\Theta\right) \tag{A.37}$$

$$s^*_{l0} = \frac{1}{4\pi}\left\{ -S_{01} r_{,l}\frac{\partial r}{\partial n}\frac{\partial r}{\partial n^{\mathrm{i}}} + S_{02} n^{\mathrm{i}}_l \frac{\partial r}{\partial n} - S_{03}\left[-n_l \frac{\partial r}{\partial n^{\mathrm{i}}} + r_{,l}\left(\mathbf{n}\cdot\mathbf{n}^{\mathrm{i}}\right)\right]\right\} \tag{A.38}$$

$$s^*_{lk} = \frac{\mu}{4\pi}\left\{ S_1\left[r_{,l} n^{\mathrm{i}}_k \frac{\partial r}{\partial n} - r_{,k} n_l \frac{\partial r}{\partial n^{\mathrm{i}}} - \delta_{lk}\frac{\partial r}{\partial n}\frac{\partial r}{\partial n^{\mathrm{i}}} + r_{,k} r_{,l}\left(\mathbf{n}\cdot\mathbf{n}^{\mathrm{i}}\right)\right] + S_2\left(r_{,k} n^{\mathrm{i}}_l \frac{\partial r}{\partial n} - r_{,l} n_k \frac{\partial r}{\partial n^{\mathrm{i}}}\right) + S_3 r_{,l} r_{,k}\frac{\partial r}{\partial n}\frac{\partial r}{\partial n^{\mathrm{i}}} + S_4\left[\delta_{lk}\left(\mathbf{n}\cdot\mathbf{n}^{\mathrm{i}}\right) + n_l n^{\mathrm{i}}_k\right] + S_5 n_k n^{\mathrm{i}}_l\right\} \tag{A.39}$$

$$S_1 = -\frac{\partial^2 \psi}{\partial r^2} + \frac{1}{r}\left(\frac{\partial \psi}{\partial r} + 3\frac{\partial \chi}{\partial r} - \frac{6}{r}\chi\right) \tag{A.40}$$

$$S_2 = 2\frac{\lambda}{\mu}\left[-\frac{\partial^2 \psi}{\partial r^2} + \frac{\partial^2 \chi}{\partial r^2} + \frac{1}{r}\left(\frac{\partial \psi}{\partial r} + \frac{\partial \chi}{\partial r} - \frac{4}{r}\chi\right)\right] + \frac{4}{r}\left(\frac{\partial \chi}{\partial r} - \frac{2}{r}\chi\right) - 2\frac{Q}{R}\frac{1}{J}\left(\frac{\partial \Theta}{\partial r} - \frac{1}{r}\Theta\right) \tag{A.41}$$

$$S_3 = 4\left[-\frac{\partial^2 \chi}{\partial r^2} + \frac{1}{r}\left(5\frac{\partial \chi}{\partial r} - \frac{8}{r}\chi\right)\right] \tag{A.42}$$

$$S_4 = \frac{2}{r}\left(-\frac{\partial \psi}{\partial r} + \frac{1}{r}\chi\right) \tag{A.43}$$

$$S_5 = \frac{4}{r^2}\chi + \frac{\lambda}{\mu}\frac{4}{r}\left(-\frac{\partial \psi}{\partial r} + \frac{\partial \chi}{\partial r} + \frac{2}{r}\chi\right) + \frac{\lambda^2}{\mu^2}\left[-\frac{\partial^2 \psi}{\partial r^2} + \frac{\partial^2 \chi}{\partial r^2} + \frac{2}{r}\left(-\frac{\partial \psi}{\partial r} + 2\frac{\partial \chi}{\partial r} + \frac{1}{r}\chi\right)\right] + \frac{Q}{R}\frac{1}{J}\left[-2\frac{\lambda}{\mu}\left(\frac{\partial \Theta}{\partial r} + \frac{2}{r}\Theta\right) - \frac{4}{r}\Theta + \frac{Q}{R\mu}\eta\right] \tag{A.44}$$

B Transformation of some fundamental solution terms

The following relationships and the Stokes' theorem let turn strongly singular and hypersingular surface integrals into weakly singular surface integrals and nearly singular line integrals. Most of them may also be seen in Domínguez et al. [17]. Note that Equation (B20) of [17] contained an erratum as it lacks two terms. The present Equation (B.6) corrects this.

$$\frac{\mathbf{n}\cdot\mathbf{n}^{\mathrm{i}}}{r^3} = -\frac{3}{r^3}\frac{\partial r}{\partial n}\frac{\partial r}{\partial n^{\mathrm{i}}} + \left(\boldsymbol{\nabla}\times\frac{\mathbf{r}\times\mathbf{n}^{\mathrm{i}}}{r^3}\right)\cdot\mathbf{n} \tag{B.1}$$

$$\frac{r_{,l}n_{,k} - r_{,k}n_{,l}}{r^2} = \varepsilon_{lkj}\left(\boldsymbol{\nabla}\times\frac{\mathbf{e}_j}{r}\right)\cdot\mathbf{n} \tag{B.2}$$

$$\frac{r_{,k}\left(\mathbf{n}\cdot\mathbf{n}^{\mathrm{i}}\right)}{r^2} = -\frac{n_k}{r^2}\frac{\partial r}{\partial n^{\mathrm{i}}} + \left(\boldsymbol{\nabla}\times\frac{\mathbf{e}_k\times\mathbf{n}^{\mathrm{i}}}{r}\right)\cdot\mathbf{n} \tag{B.3}$$

$$\frac{r_{,l}r_{,k}\left(\mathbf{n}\cdot\mathbf{n}^{\mathrm{i}}\right)}{r^3} = -\frac{5r_{,l}r_{,k}}{r^3}\frac{\partial r}{\partial n}\frac{\partial r}{\partial n^{\mathrm{i}}} - \frac{r_{,l}n^{\mathrm{i}}_k + r_{,k}n^{\mathrm{i}}_l}{r^3}\frac{\partial r}{\partial n} + \left[\boldsymbol{\nabla}\times\left(r_{,l}r_{,k}\frac{\mathbf{r}\times\mathbf{n}^{\mathrm{i}}}{r^3}\right)\right]\cdot\mathbf{n} \tag{B.4}$$

$$\frac{n_k}{r^3} = \frac{3r_{,k}}{r^3}\frac{\partial r}{\partial n} + \left(\boldsymbol{\nabla}\times\frac{\mathbf{r}\times\mathbf{e}_k}{r^3}\right)\cdot\mathbf{n} \tag{B.5}$$

$$\frac{r_{,l}r_{,k}r_{,j}\left(\mathbf{n}\cdot\mathbf{n}^{\mathrm{i}}\right)}{r^2} = -\frac{1}{3}\frac{r_{,j}n_k n^{\mathrm{i}}_l}{r^2} - \frac{1}{3}\frac{r_{,l}n_k n^{\mathrm{i}}_j}{r^2} + \delta_{lk}\frac{1}{3}\frac{r_{,j}\left(\mathbf{n}\cdot\mathbf{n}^{\mathrm{i}}\right)}{r^2} + \delta_{jk}\frac{1}{3}\frac{r_{,l}\left(\mathbf{n}\cdot\mathbf{n}^{\mathrm{i}}\right)}{r^2} - \frac{r_{,l}r_{,j}n_k}{r^2}\frac{\partial r}{\partial n^{\mathrm{i}}} + \frac{1}{3}\left[\boldsymbol{\nabla}\times\left(r_{,l}r_{,j}\frac{\mathbf{e}_k\times\mathbf{n}^{\mathrm{i}}}{r}\right)\right]\cdot\mathbf{n} \tag{B.6}$$

References

[1] Ahmad S, Irons BM, Zienkiewicz OC (1970) Analysis of thick and thin shell structures by curved finite elements. Int J Numer Meth Eng 2(3):419–451

[2] Arany L, Bhattacharya S, Macdonald J, Hogan SJ (2015) Simplified critical mudline bending moment spectra of offshore wind turbine support structures. Wind Energy 18:2171–2197

[3] Ariza MP, Domínguez J (2002) General BE approach for three-dimensional dynamic fracture analysis. Eng Anal Bound Elem 26:639–651

[4] Basu U, Chopra AK (2003) Perfectly matched layers for time-harmonic elastodynamics of unbounded domains: theory and finite-element implementation. Comput Method Appl M 192:1337–1375

[5] Bathe KJ, Dvorkin EN (1986) A formulation of general shell elements – the use of mixed interpolation of tensorial components. Int J Numer Meth Eng 22:697–722

[6] Biot MA (1956) Theory of propagation of elastic waves in a fluid-saturated porous solid. I. Low-frequency range. J Acoust Soc Am 28(2):168–178

[7] Bonnet G (1987) Basic singular solutions for a poroelastic medium in the dynamic range. J Acoust Soc Am 82(5):1758–1762

[8] Bordón JDR, Aznárez JJ, Maeso O (2014) A 2D BEM-FEM approach for time harmonic fluid-structure interaction analysis of thin elastic bodies. Eng Anal Bound Elem 43:19–29

[9] Bordón JDR, Aznárez JJ, Maeso O (2016) Two-dimensional numerical approach for the vibration isolation analysis of thin walled wave barriers in poroelastic soils. Comput Geotech 71:168–179

[10] Bougacha S, Tassoulas JL (1991) Seismic analysis of gravity dams I: modeling of sediments. J Eng Mech-ASCE 117(8):1826–1837

[11] Bucalem ML, Bathe KJ (1993) Higher-order MITC general shell elements. Int J Numer Meth Eng 36:3729–3754

[12] Buchanan JL, Gilbert RP (1997) Transmission loss in the far field over a one-layer seabed assuming the biot sediment model. J Appl Math Mech 2:121–135

[13] Burton AJ, Miller GF (1971) The application of integral equation methods to the numerical solution of some exterior boundary-value problems. P R Soc London 323:201–210

[14] Cheng AHD, Badmus T, Beskos DE (1991) Integral equation for dynamic poroelasticity in frequency domain with BEM solution. J Eng Mech-ASCE 117(5):1136–1157

[15] Domínguez J (1991) An integral formulation for dynamic poroelasticity. J Appl Mech 58:588–591

[16] Domínguez J (1992) Boundary element approach for dynamic poroelastic problems. Int J Numer Meth Eng 35:307–324

[17] Domínguez J, Ariza MP, Gallego R (2000) Flux and traction boundary elements without hypersingular or strongly singular integrals. Int J Numer Meth Eng 48:111–135

[18] Dvorkin EN, Bathe KJ (1984) A continuum mechanics based four-node shell element for general nonlinear analysis. Eng Computation 1:77–88

[19] Gallego R, Domínguez J (1996) Hypersingular BEM for transient elastodynamics. Int J Numer Meth Eng 39:1681–1705

[20] Geuzaine C, Remacle JF (2009) Gmsh: a three-dimensional finite element mesh generator with built-in pre- and post-processing facilities. Int J Numer Meth Eng 79(11)

[21] Hong HK, Chen J (1988) Derivations of integral equations of elasticity. J Eng Mech-ASCE 114(6):1028–1044

[22] Kassir MK, Xu J (1988) Interaction functions of a rigid strip bonded to saturated elastic half-space. Int J Solids Struct 24(9):915–936

[23] Kaynia AM, Kausel E (1982) Dynamic stiffness and seismic response of pile groups. Research Report R83-03, Massachusetts Institute of Technology, Cambridge, MA

[24] Lee PS, Bathe KJ (2004) Development of MITC isotropic triangular shell finite elements. Comput Struct 82:945–962

[25] Liingaard M, Andersen L, Ibsen L (2007) Impedance of flexible suction caissons. Earthq Eng Struct D 36:2249–2271

[26] Lin CH, Lee VW, Trifunac MD (2005) The reflection of plane waves in a poroelastic half-space saturated with inviscid fluid. Soil Dyn Earthq Eng 25:205–223

[27] Maeso O, Aznárez JJ, Domínguez J (2004) Three–dimensional models of reservoir sediment and effects on the seismic response of arch dams. Earthq Eng Struct D 33(10):1103–1123

[28] Maeso O, Aznárez JJ, García F (2005) Dynamic impedances of piles and groups of piles in saturated soils. Comput Struct 83:769–782

[29] Manolis GD, Beskos DE (1989) Integral formulation and fundamental solutions of dynamic poroelasticity and thermoelasticity. Acta Mech 76(1-2):89–104

[30] Mantič V (1993) A new formula for the C-matrix in the Somigliana identity. J Elasticity 33:191–201

[31] Mantič V, París F (1995) Existence and evaluation of the two free terms in the hypersingular boundary integral equation of potential theory. Eng Anal Bound Elem 16:253–260

[32] Marburg S (2008) Computational Acoustics of Noise Propagation in Fluids - Finite and Boundary Element Methods, chapter 11. Discretization Requirements: How many Elements per Wavelength are Necessary?, pages 309–332. Springer

[33] Messner M, Schanz M (2011) A regularized collocation boundary element method for linear poroelasticity. Comput Mech 47:669–680

[34] Messner M, Schanz M (2012) A symmetric Galerkin boundary element method for 3d linear poroelasticity. Acta Mech 223:1751–1768

[35] Mi Y, Aliabadi MH (1992) Dual boundary element method for three-dimensional fracture mechanics analysis. Eng Anal Bound Elem 10:161–171

[36] Oñate E (2013) Structural Analysis with the Finite Element Method. Linear Statics, volume 2: Beams, Plates and Shells. CIMNE - Springer

[37] Padrón LA, Aznárez JJ, Maeso O (2007) BEM-FEM coupling model for the dynamic analysis of piles and pile groups. Eng Anal Bound Elem 31:473–484

[38] Parish H (1979) A critical survey of the 9-node degenerated shell element with special emphasis on thin shell application and reduced integration. Comput Method Appl M 20:323–350

[39] Portela A, Aliabadi MH, Rooke DP (1992) The dual boundary element method: effective implementation for crack problems. Int J Numer Meth Eng 33:1269–1287

[40] Stolarski H, Belytschko T (1982) Membrane locking and reduced integration for curved elements. J Appl Mech 49:172–176

[41] Tadeu A, António J, Amado P, Godinho L (2007) Sound pressure level attenuation provided by thin rigid screens coupled to tall buildings. J Sound Vib 304:479–496

[42] von Estorff O (2000) Boundary Elements in Acoustics. WIT Press

[43] Wrobel LC, Aliabadi MH (2002) The Boundary Element Method. Wiley

[44] Yang HTY, Saigal S, Masud A, Kapania RK (2000) A survey of recent shell finite elements. Int J Numer Meth Eng 47:101–127

[45] Zienkiewicz OC, Taylor RL (2005) The Finite Element Method. Butterworth-Heinemann, 6 edition